Technische Universität München
Fakultät für Maschinenwesen
Lehrstuhl für Mikrotechnik und Medizingerätetechnik
Univ.-Prof. Dr. Tim C. Lüth

Diplomarbeit

Labeled Needle Rendering Solution for Image Guided Brachytherapy

Guillaume Pernelle

Matr.-Nr.: 3290614

Betreuender Hochschullehrer:	Prof. Dr. rer. nat. Tim C. Lüth
Betreuer:	Dr.-Ing. Franz Irlinger, Dr. Tina Kapur, Dr. Dr. Jan Egger und Dr. Yi Gao
Ausgegeben am:	15.06.2012
Abgegeben am:	14.12.2012

Ehrenwörtliche Erklärung

Ich erkläre hiermit ehrenwörtlich, dass ich die vorliegende Arbeit selbstständig und ohne Benutzung anderer als der angegebenen Hilfsmittel angefertigt habe; die aus fremden Quellen (einschließlich elektronischer Quellen) direkt oder indirekt übernommenen Gedanken sind ausnahmslos als solche kenntlich gemacht.

Garching bei München, den 14. Dezember 2012 _____

Abstract

There is increasing evidence of the value of using medical imagery to guide therapy of various types of malignancies. This thesis focuses on image analysis techniques to support therapy of gynecologic cancer. Gynecologic cancers involve malignancies of the uterus, cervix, vagina/vulva, and the ovaries. Treatment of gynecologic cancers typically involves radiation therapy in two steps: first external beam radiation, and then brachytherapy in which applicators are used to place radiation isotopes directly in the tumor. Magnetic resonance imagery is widely used worldwide to diagnose gynecological cancers, and is in the early stages of being used also for placement of applicators and treatment planning. The contribution of this thesis is in the area of image analysis techniques for registration and segmentation of image-guided gynecological cancer therapy.

Two computational algorithms have been introduced in this thesis: registration of the applicator, and extraction of the needles. This work has been released for public use in a new open-source software module that integrates efficiently with clinical workflow.

All methods are described in details in this thesis and are evaluated with phantom and real patient data from cases performed in the Advanced Modality Image-Guided Operating (AMIGO) suite of the Brigham & Women's Hospital.

Garching bei München, December 2012 Guillaume Pernelle

Acknowledgements

Above all, I would like to thank Professor Dr. Tim C. Lüth, chairman of the department of Micro and Medical Technologies (MiMed), Dr. Franz Irlinger, my supervisor at the Technische Universität München, and Professor Dr. Ron Kikinis, director of the Surgical Planning Laboratory, for the trust they placed in me and for their support through this great opportunity. Writing this thesis at the Surgical Planning Laboratory in Boston was an amazing experience that I am deeply grateful for.

I am especially indebted to my advisors at the Brigham & Women's Hospital (Harvard Medical School affiliate), Dr. Tina Kapur, Dr. Dr. Jan Egger and Dr. Yi Gao for their exceptional guidance throughout this work. I was really fortunate having Tina as advisor. She has the gift of providing an always stimulating and challenging environment and her dedication to her students is truly rare. Her great advice will indubitably continue to inspire me in research as in life and I will always remember her warm welcome. To have Jan as mentor greatly contributed to the success of this project. His great ideas, feedback and his rousing unbreakable love for research have been guiding forces all along this project. Working with Yi and having him as mentor was also an experience I am deeply grateful for. I learned from him the importance of methodology and patience in the algorithm development. I am especially thankful that he showed so much interest in my work and for his optimism.
Then, I would also like to thank Dr. Akila Viswanathan for her great help and understanding as well as Janice Fairhust and Dr. Antonio Damato to whom I owe the data and materials that have made this project possible. I am also very lucky to have met Dr. Williams Wells who helped me in many ways during this thesis and will remain a great source of inspiration for me.

I have been very fortunate to evolve in an extremely stimulating, productive and supportive research environment. An ongoing thank you goes to the members of the Surgical Planning Laboratory: Xiaojun Chen, Tobias Penzkopfer, Paul Mercea, Andrey Fedorov, Neha Agrawal, Sarah Parisot, Nabgha Farhat, Tobias Lüddermann, Alireza Mehrtash, Rie Oyama, Marianna Jakab, Robert McKie, Sonia Pujol, Laurent Chauvin, Petter Risholm, Jayender Jagadeesan, Junichi Tokuda, Atsushi Yamada, Sang-Eun Song, Ehud Schmidt, for all their help and support throughout my time here. I am further grateful to everyone in the amazing Slicer community, especially Jean-Christophe Fillon-Robin, Steve Pieper and Julien Finet for their essential advice and all the help they gave me.

Finally, I would like to thank my family and my girlfriend for their unconditional love and support.

Contents

1 Introduction

Gynecological cancers, which consist of cervical, endometrial, and vaginal/vulvar cancers, remain the fourth largest cause of death among women in the US since 2010, with reports of 88,750 (5.6% increase) new cases and 29,520 (6.5% increase) deaths per year in 2012 [1].

There is an increasing interest in expanding the role of MRI beyond diagnosis and into brachytherapy treatment planning as well as in applicator placement because of early results indicating that it may lead to more precise treatment of the tumor and a reduction in the radiation dose to healthy tissue [2, 3]. This thesis presents a method for robust localization of the brachytherapy applicator in intra-operative Magnetic Resonance (MR) imagery by alignment with its CAD model. This alignment allows us to estimate and visualize the insertion of "virtual needles" prior to the actual insertion. Moreover this thesis presents a needle localization method, which can extract curved or straight needle with a high accuracy in a short time.

1.1 Background

In the early twentieth century, shortly after it was found that radiation caused tumors to shrink [4], Henri-Alexandre Danlos at the Curie institute in Paris and Robert Abbe at the St Luke's and Memorial Hospital in New York, started developing techniques to use the radiation to treat tumors with internal radiotherapy. However, observed consequences of radiation exposure to operators from handling manually radioactive sources did slow down its use in a first time. The development of remote after-loading systems allowing the radiation to be delivered from a shielded safe in the 1950s and 1960s and more recently, 2D real-time or 3D imaging modalities have made brachytherapy a safe and effective method to treat cervical, prostate, breast and skin cancers.

Brachytherapy can be classified as temporary or permanent. In the first case, the radiation source is placed to the targeted tissue for only few minutes to few hours. An applicator is surgically placed in region needing treatment, and then the sources are loaded. Thus, the radiation only affects a specific area, thereby minimizing the exposure of healthy tissue to radiation. Permanent brachytherapy involves placing and leaving small radioactive seeds in the treatment area. The level of radiation emitted by the sources will gradually decline over weeks or months to almost zero.

The radiation dose rate absorbed by surrounding medium is the second parameter to take into consideration. Expressed in Grays per hour (Gy/h), it varies from low-dose rate (LDR, up to 2 Gy/h) to medium-dose rate (MDR, between 2 and 12 Gy/h) and high-dose rate (HDR, exceeding 12 Gy/h). It also includes pulsed dose rate involving short pulses of radiation.

HDR treatments, developed in the late 1960s offers the advantage of shorter treatment times (a few minutes or hours rather than days), although the treatments have to be fractioned and overall treatment time is not necessarily shortened.

An accurate placement of sources allows the use of higher dose rate and lowers the risk of damaging healthy tissue. Moreover a high level of dose conformity through accurately targeting ensures that the whole tumor receives an optimal level of radiation, thus increasing the chance of cure and preservation of organ functions.

In order to deliver the best precision of the target localization and therefore an optimal dose radiation, brachytherapy is combined with medical imaging. Image-guided radiation therapy (IGRT) refers to radiation treatment guided by imaging modalities such ultrasound (US), computed tomography (CT), positive emission tomography (PET), magnetic resonance imaging (MRI) which assist the radiation oncologist during the positioning of the catheters (assimilated as "needles" or "applicators" in the rest of this thesis).

HDR version of after-loading machines were introduced in the mid-1980s and in late 1980s were developed HDR after-loading machines, such as the microSelectron-HDR, in which a single source of iridium-192 (containing typically an activity if 370 to 740 GBq) is sequentially stepped through a series of dwell positions in all the treatment applicators in turn. These machines have a computer control station outside the shielded treatment room. The single iridium source is contained in a tungsten-shielded safe in the head of the machine. The source capsule is laser welded to a long drive cable, which is connected to a stepper motor which can position the source into the treatment channel in up to 48 dwell positions with an accuracy of ± 1 mm. The spacing between the positions is either 2.5 mm or 5 mm, thereby treating a maximum length of 235 mm. The exposure time can be different at each position. Thus, the large combination of dwell positions and times can produce complex dose distribution. Moreover, the source of 'stepping source' machines presents another advantage over the older machines based caesium or cobalt source trains. The high specific activity of iridium-192 permits the source, and therefore the applicator to have a small diameter. Typically the source has a diameter of 0.5 mm and the applicators have an external diameter of 2 mm. Thus, applicators are thin and flexible and can be used in body sites not otherwise accessible such as the bronchus or bile duct [5].

1.2 Thesis Outline

Today most clinical hospitals perform gynecological brachytherapy under 2D X-ray or US guidance. Leading teaching hospitals have pioneered the use of 3D images for this task.

In this thesis, image analysis, algorithms and software have been developed to assist in 3D MR guidance gynecological brachytherapy at Brigham and Women’s Hospital, a teaching hospital of Harvard Medical School. In particular, key contributions of this thesis are segmentation of the needles from MR images and labeling of these needles in a method familiar to physicians by performing registration of CAD models of gynecological applicator to their MR images.

Chapter 2 describes prior work in the field, chapter 3 details the approach developed in this thesis and chapter 4 presents results, discusses them and summarizes conclusions and area for future research.

2 Prior Work

To the best of our knowledge, the method we present in this thesis is the first for labeled needle rendering in MR images for brachytherapy. However, closely relative work has been done for needle detection mainly in US images. In this chapter we review the methods used for needle detection or other related fields and discuss their connection with our needle detection and labeling task.

Needle artifact detection from MRI has primarily been pursued in the context of MR-guided interventions such as biopsy or radio-frequency ablation, where the value of this step in making complex procedures feasible has been presented in detail in the 2010 textbook by computer scientists Kevin Cleary and Terry Peters [6].

Use of Magnetic Resonance Imaging for Needle Localization

Radiologist Lewin and his team at Johns Hopkins University demonstrated in 1999 that in contrast to guidance using x-ray based imaging where the material of the needle is the main factor that influences its visibility, the success of this task when using MRI is additionally heavily dependent on the MR imaging parameters, the sensitivity of the imaging sequence to magnetic susceptibility effects, and the direction of the needle relative to the MRI frequency encoding [7]. These observations motivated us to work closely with MR physicists in order to obtain optimal imaging sequences, and as a result of this collaboration, Dr. Ehud Schmidt, a leading MR physicist in our institution developed the b-SSFP imaging sequence for this project.

In 2006, computer scientist DiMaio carefully quantified differences in the needle tip locations from MR sequences optimized for susceptibility imaging based on the shaft orientation demonstrated a 4-5 mm change when the direction of the needle was parallel vs. perpendicular to the direction of the static magnetic field [8]. This prompted us to carefully compare the results of our MR based needle localization to CT images, in which no such distortion appears. Fortunately in our application, the direction of the needles is similar (not parallel, but in the same general direction) to the magnetic field orientation, which leads to clinically acceptable geometric localization artifact. A comparison between CT and MR images of the same sample has confirmed this observation, and is presented in the results section of this document.

Post-processing Magnetic Resonance Images for Needle Segmentation

Hough Transform approaches have been used successfully for linear needle segmentation in ultrasound images, as Ding and al. demonstrated in 2003 [9]. However it is repeatedly suggested in the literature that this step could use improvement because needles often bend as they are inserted in the body. Indeed the flexibility of the fine needles and the density variability of the tissues surrounding the target make it difficult to predict the behavior of the needle over the course of the insertion and a perfectly straight-line insertion cannot be assumed. Furthermore, it also may appear that at some point of a case the radiation oncologist bends needles on purpose to access specific areas. This incited us to consider the following research projects on curve detection.

Okazawa et al. [10] presented in 2006 a method based on edge-detection and Hough Transform. The Hough Transform is used to obtain the best straight-line candidate, which

allows defining a narrow window. Then an edge-detection filter on this region-of-interest provides a set of points expected to fall on the real needle shaft. A polynomial regression fits a curve to the needle data, thus capturing the bent needle shape. However, in some cases the needle deflection is substantially great and the linear feature detection capabilities of the standard Hough transform may not be effective in locating the needles. For this reason they proposed another method, enhancing the Hough transform, using an empirical model for needle behavior in tissue. It assumes that the needle curvature can be estimated as a constant curvature.

Another approaches combine Extended Kalman Filtering used for tracking sequences of position (coordinates of features points) [11] with a Hough voting scheme that extracts optimal parameters of curves passing through image points. As part of the process in Velastin and Xu's method [12], a Mahalanobis Distance [13] test is computed to reject outliers, so the points far from the candidate line do not contribute to voting or refinement, incorporating this way a noise model dealing with "errors in the variable". This robust method leads to high accuracy and low computation time through the Extended Kalman Filter that helps to predict the future state.

While developing a method for automatic segmentation of spinal nerve bundles [14], Dalca proposed an approach to obtain a flexible statistical particle representation of tubular structures based on Bézier splines. Segments, or particles, of tubular bundles are iteratively tracked, weight based on how well they describe the corresponding MRI patch. A set of point probability masses represents a likelihood of a nerve at a specific location. This likelihood is then propagated onto the next patch during the next iteration. As of a result, the nerve direction and thickness are tracked.

Needle trajectory detection based on "vesselness" value has also been implemented in Tibrewal's master thesis [15]. The Hessian based 3D Frangi filter is applied to extract tubular structures in a predefined area of 3D MR images.

Hough Transform

The Hough transform is a feature extraction technique which first was applied to the identification of straight lines in images and then was extended to detect arbitrary shapes, most commonly circles and ellipses and was renamed "Generalized Hough Transform" (GHT) [4,5]. (This method is used in the applicator registration method of this thesis, that is described in the next chapter.) The image is transformed into a parameter space called Hough space, where each cell represents a possible object location. Depending on the target object, a voting procedure fills the Hough space with votes for possible object location. Due to the voting procedure, this is a robust method against image noise and occlusion or missing parts, which makes it particularly appropriated for medical image processing.

Let O be the origin at the upper left corner of the image (a 2D axial slice or the MR volume). Let R be the radius of a circle, m, n its coordinates in x and y directions respectively. This circle can be represented by the following equations where equation (1) relates to Cartesian space while equations (2) and (3) to Parametric space.

$$(x - m)^2 + (y - n)^2 = R^2 \quad (1)$$

$$x = m + R.\cos(\theta) \quad (2)$$

$$y = n + R.\sin(\theta) \tag{3}$$

$$m = R.\cos(\theta) - x \tag{4}$$

$$n = R.\sin(\theta) - y \tag{5}$$

$$n = m.\tan(\theta) - x.\tan(\theta) + y \tag{6}$$

The Hough space $\mathcal{H}$, or parameter space, is defined by:

$$(R, m, n) \in \left[R_{min}, R_{\max}\right)\times[0; x_{max}]\times[0; y_{max}]$$

$\mathcal{H}$ is then divided into a discrete number of accumulator cells that can collect votes, forming the accumulator space $\mathcal{A}$ (Figure 5).

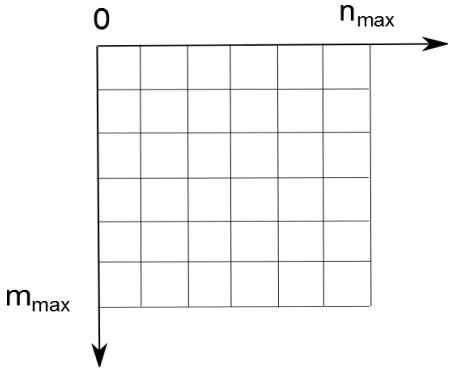

Fig. 1 Accumulator space $\mathcal{A}$

For a R given, $\mathcal{A}$ is filled with zeros. Then a pre-processing operation is computed by edge-detectors like Sobel filters or by morphological operations. Then, for each point (x, y) the gradient (or edge) magnitude $\mathrm{G}(x, y)$ is computed and for each point in $\mathrm{G}(x, y)$, the value of the points in $\mathcal{A}(x, y)$ on the circle (6) are incremented. The peaks in the accumulator space mark the equations of significant circles Fig. 2.

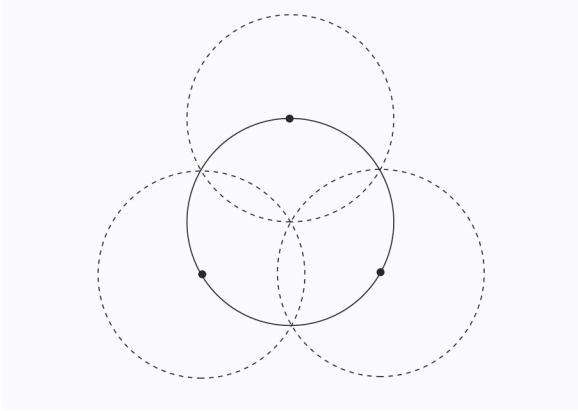

Fig. 2 The contribution of the edge points to the accumulator space $\mathcal{A}$

Iterative Closest Points Registration

The *iterative closest point registration* (ICP) [16] is a robust technique to register free form surfaces with high precision. This is used for registration of surface models in the applicator registration step in the next chapter.

The goal of ICP is to determine the rigid transformation **T** that best aligns a cloud of scene points $\mathcal{S}$ with a geometric model $\mathcal{M}$. The alignment process works to minimize the distance (mean squared or absolute) between model points and their nearest scene point. ICP is efficient, with average case complexity of $O(n \log n)$ for n point images, and it converges monotonically to a local minimum. For each iteration, the algorithm computes correspondences by finding nearest points, and then minimizes the error (mean square or absolute) in position between the correspondences [1,2]. A good initial estimate of the transformation is required, otherwise it will converge to a local optimum solution, and all scene points are assumed to have correspondences in the model. The algorithm can also be understood as follows:

Let $\mathcal{S}$ be a set of N_s points $\{s_1, \dots, s_{N_s}\}$ and let $\mathcal{M}$ be the model. Let $\|s - m\|$ be the distance between point $s \in \mathcal{S}$ and $m \in \mathcal{M}$, and let $\mathrm{CP}(s_i, \mathcal{M})$ be the closest point in $\mathcal{M}$ to the scene point s_i.

1. Let $\mathbf{T_0}$ be an initial estimate of the transformation.
2. Repeat for $k = 1..k_{max}$ or until termination criteria is met.
   (a) Build up the set of correspondences $C = \bigcup_{i=1}^{N_s} \{(\mathbf{T}_{k-1}(s_i), \mathrm{CP}(\mathbf{T}_{k-1}(s_i), \mathcal{M}))\}$
   (b) Compute the new transformation $\mathbf{T}_k$ that minimizes mean square error between point pairs in C[1,2,3].

Open-source platform 3D Slicer

In preliminary work, a software module for MR-guided gynecologic brachytherapy has been developed for the established 3D Slicer open source software platform [17] using well-regarded toolkits in computer graphics and medical image processing such as VTK, ITK, CTK, and QT. A semi-automatic registration method was present to register the CAD template model to the MRI image volume.

3D Slicer [18] is a free and open source software package for medical image analysis and visualization. iGyne is a 3D Slicer Qt-scripted module designed for MR-guided interstitial brachytherapy planning for gynecologic cancer in AMIGO at the Brigham and Women's Hospital. Use of the iGyne in AMIGO included the following steps 1) Loading of CAD models of the interstitial template and obturator, 2) MR scan of the patient with the template positioned to 3D Slicer using the DICOM protocol, 3) an initial rigid registration is computed from 3 corresponding point pairs provided by the user on the template holes, 4) the registration is refined using the Iterated Closest Point [16] algorithm for rigid registration, 5) optionally, segmentation and visualization of 3D models of the tumor are obtained rapidly using editing capabilities of 3D Slicer, and 6) finally, virtual needles are selected on a schematic of the template and rendered in the 2D and 3D views, with the insertion depth independently adjustable for each needle. This allows for ease of visualization of spatial

relationships among the needles, tumors, and surrounding anatomical structures can be clearly observed, and hence ease in determination of the optimal number and positions of the needles, as well as insertion depth.

As a prototype, this first version of iGyne demonstrated the feasibility of this project. Then it was planed to add some features and the importance of making it portable was greatly emphasized. The 3D Slicer environment's capabilities offered the opportunity to go through, what Professor Dr. Ron Kikinis likes to call "The Valley of Death", separating the software prototype stage from the software tool stage, where translational research is possible and where it can be proven that a software tool is worth doing.

With the prototype version of iGyne, from the moment when the data are loaded, to the needle planning part, it took around ten minutes. The user had to navigate back and forth between more than seven different modules (load data, annotation, fiducial registration, crop volume, editor, models, iGyne) and had to respect a really strict workflow, meaning only fully experimented user could use it.

Thus, the first goal of the new version of iGyne was to design and build a single module with a simple workflow, allowing the user to intuitively perform the same task and requiring a minimal amount of user interaction, automating every step that could be. On this purpose it has been chosen to work with the CTK class *ctkWorkflowWidget* available in the Python CTK library. The Python integration in 3D Slicer allows easy prototyping and easy access to the different modules available, from any module. Another advantage is the no-need of code compilation which makes it easy to share and test on several machines and OS environment.

Then, the registration of the CAD model of the gynecological applicator to its MR image was neither robust nor accurate enough. Indeed, it only used the information provided by the template in the image. The dimensions of the template, with its small height (Z-axis) relative to its width (X-axis) and length (Y-axis), makes that the information along the Z-axis is not sufficient or weighted equally in the registration process, thus leading to an important registration error.

The second part of this thesis was to improve the registration by including the information provided by the obturator. Segmentation and registration methods were investigated to do so, as for example threshold segmentation, interactive GrowCut segmentation, simple region growing segmentation or customized Hough transform detection for the segmentation.

In the same time, Gao's work on straight needle detection has been integrated. Following the observation made during the Summer Project Week 2012 at the Massachusetts Institute of Technology (MIT) organized by the National Alliance for Medical Image Computing (NA-MIC), that a neural tractography approach could be used to segment needles (assimilated as a single branch neural tract) in magnetic resonance images, Gao has developed an algorithm extracting straight needles [19].

Having at disposition a reliable registration and segmented needles, the next step was to label these needles accordingly to their associated real needle.

Some missing features have also been added, as the integration of a DICOM importation feature allowing a robust and fast transfer between magnetic resonance scanner and the computer executing the software, or needle-managing and displaying options.

All the software development has been done considering the importance of its future portability. As a result, iGyne has been developed and integrated into Slicer as an extension available through the Slicer "AppStore" (extension manager). Thus it is now available on every computer able to run Slicer, as well as on Windows, Linux or Mac OS X environments (http://download.slicer.org/). Sample data of a phantom study has been included to let the user tries it easily and moreover, real gynecological patient MRI datasets are available at http://www.spl.harvard.edu/publications/item/veiw/2227/.

3 Approach

The goal of this thesis is to provide radiation oncologists, through a graphical user-friendly interface, information that helps them localize the brachytherapy applicator under MR imaging. It proposes the combination of an appropriate imaging sequence that enhances the appearance of individual needle tips that are otherwise challenging for the physician to see, with post-processing that prompts him/her to click once on each needle tip, and presents (within one minute) accurate 3D labeled renderings of the entire applicator assembly.

The key algorithmic contributions of this thesis are in needle segmentation and applicator registration, and are detailed in section 3.1 and 3.2, respectively. Section 3.3 presents software development contributions, introducing iGyne v2.0, a python scripted module integrated in the open-source and multiplatform software 3D Slicer.

3.1 Needle segmentation in MR images

3.1.1 **3D b-SSFP MRI sequence**

A 3D-b-SSFP sequence has been optimized by MR physicists at Harvard Medical School and Brigham and Women's Hospital for use in this project and was reported in [20]. The deployment of this sequence has enabled the physician to rapidly identify the tip of the needle because of the distinct "*figure 8*" shaped ballooning artifacts. Fig. 3 illustrates this point. Note that compared to fat-suppressed 3D-FSE images that were in use prior to this b-SSFP sequence availability (shown in the first column, images A and C which show sagittal and axial cross-sections), the needle artifacts in b-SSFP are much more pronounced and easy to distinguish from signal voids due to anatomical structures (shown in images B and D of Figure 1).

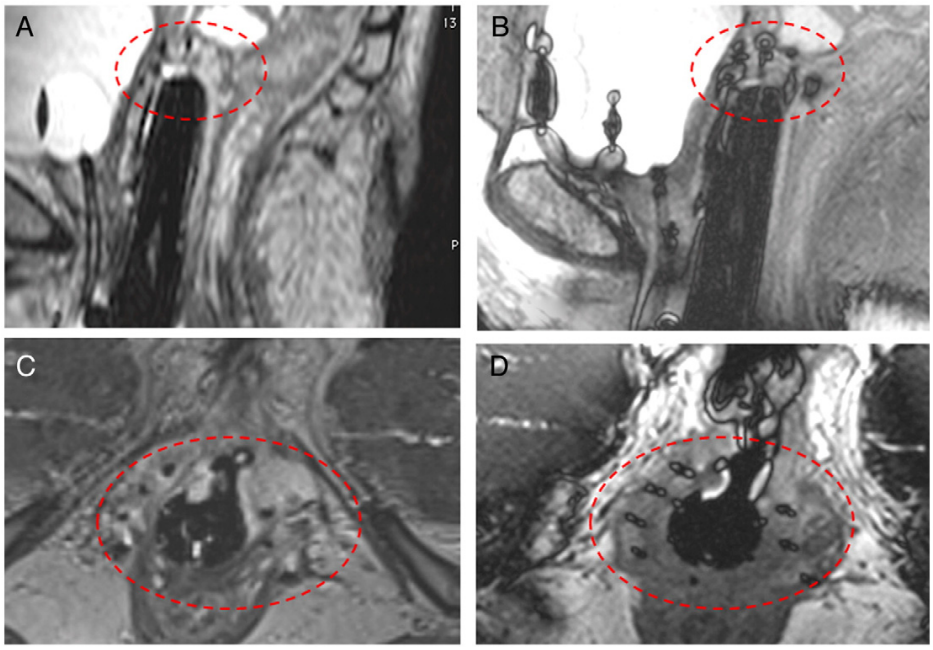

Fig. 3 Note that compared to fat-suppressed 3D-FSE images that were in use prior to this b-SSFP sequence availability (shown in the first column, images A and C which show sagittal and axial cross-sections), the needle artifacts in b-SSFP are much more pronounced and easy to distinguish from signal voids due to anatomical structures (shown in images B and D) [20].

3.1.2 **Linear Needle Segmentation**

At a national image-guided therapy workshop hosted at Harvard Medical School in September 2012 [19], we reported a method to extract and display linear approximations to brachytherapy needles from the b-SSFP MRI sequence described above. The algorithm requires one click on any part of each needle from the user based on which it constructs 3D models for up to 20 needles in less than a minute. The algorithm constructs a needle feature image (computed from second derivatives of image intensities) from the MRI and the desired needle trajectories are then computed as the path along which the needle feature is maximized.

Fig. 4 shows that the result of needle extraction using this method. This dataset contains more than 10 needles but only 3 are shown for clarity of visualization).

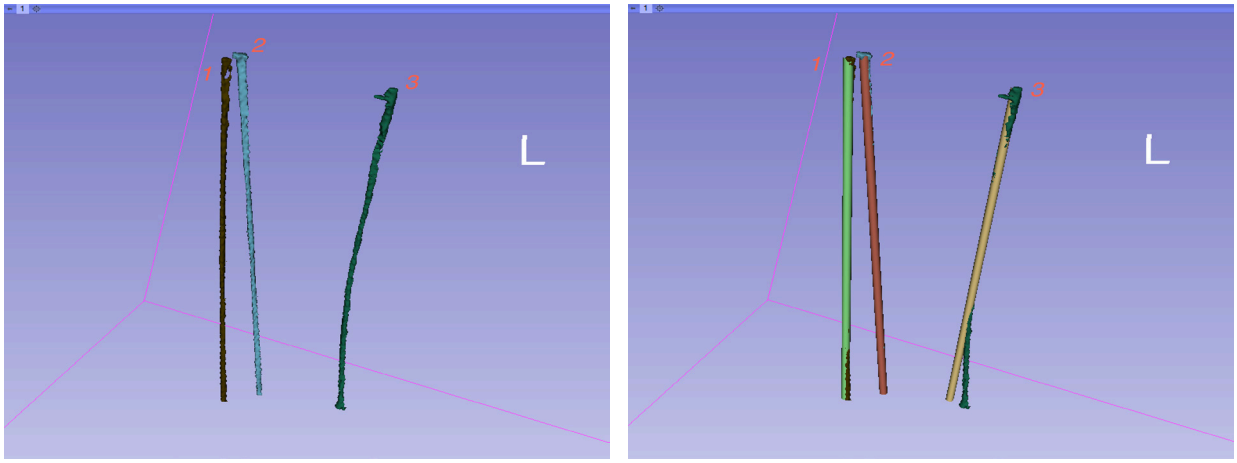

Fig. 4 Left: results of the manual segmentation done by an expert. Right: results of the linear needles extraction superposed with the manual segmented needle. Different colors have been chosen to emphasize the differences between both segmentations.

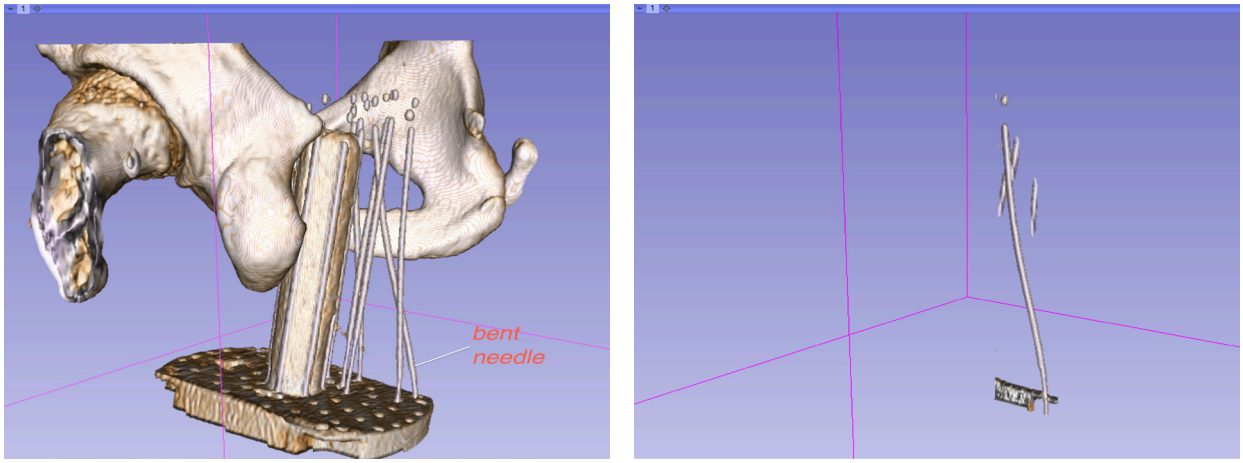

Fig. 5 Left: Volume rendering of a computer tomography scan. The pelvic structure is shown, as well as the gynecological applicator. Right: the isolated needle is an example of a needle that cannot be extracted with the linear extraction algorithm, because of its two inflexion points.

Illustrated in Fig. 4, needle 3 is a needle that cannot be extracted correctly using this linear approximation because it is bent. The error shown here is not critical. However, if the deflection is great, close to the tip of the needle, in most of the cases the algorithm will simply fail to detect the needle, as for the represented case in Fig. 5 and Fig. 6. This motived the introduction of needle extraction method described in the next section.

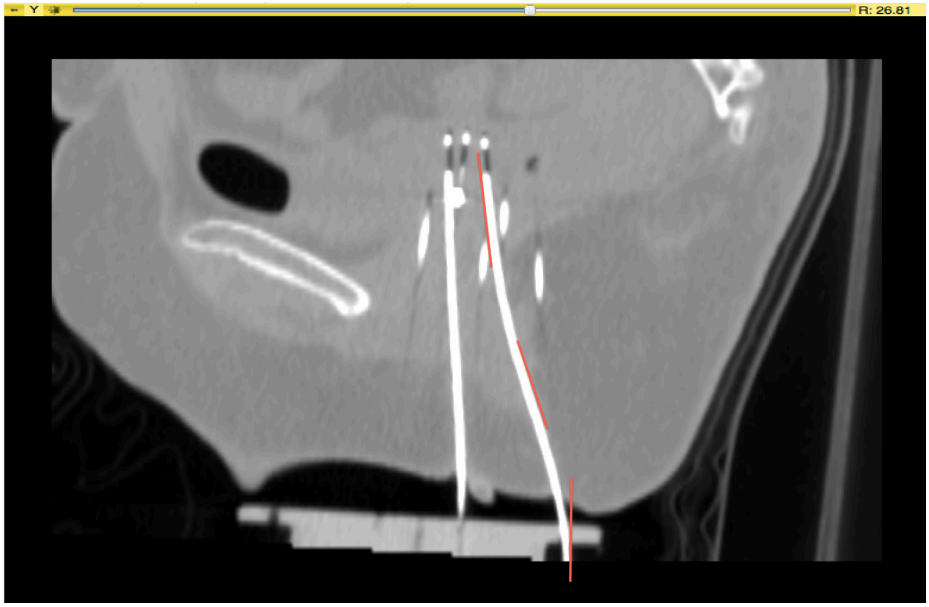

Fig. 6 Sagittal views of a CT scan. The needle on the left presents two inflexion points, which makes it difficult to be accurately extracted with a linear extraction algorithm.

3.1.3 **Curved Needle Extraction**

In some cases, the needle deflection due to the bending is too great to extract a valid linear approximation. Indeed, the radiation oncologist may have to bend the needle prior to insertion to avoid the organ-at-risks or the bones of the pelvis, as shown in Fig. 7.

Therefore, a second method has been developed that is described in this section. Fig. 8 introduces the idea that was implemented and some of the main parameters.

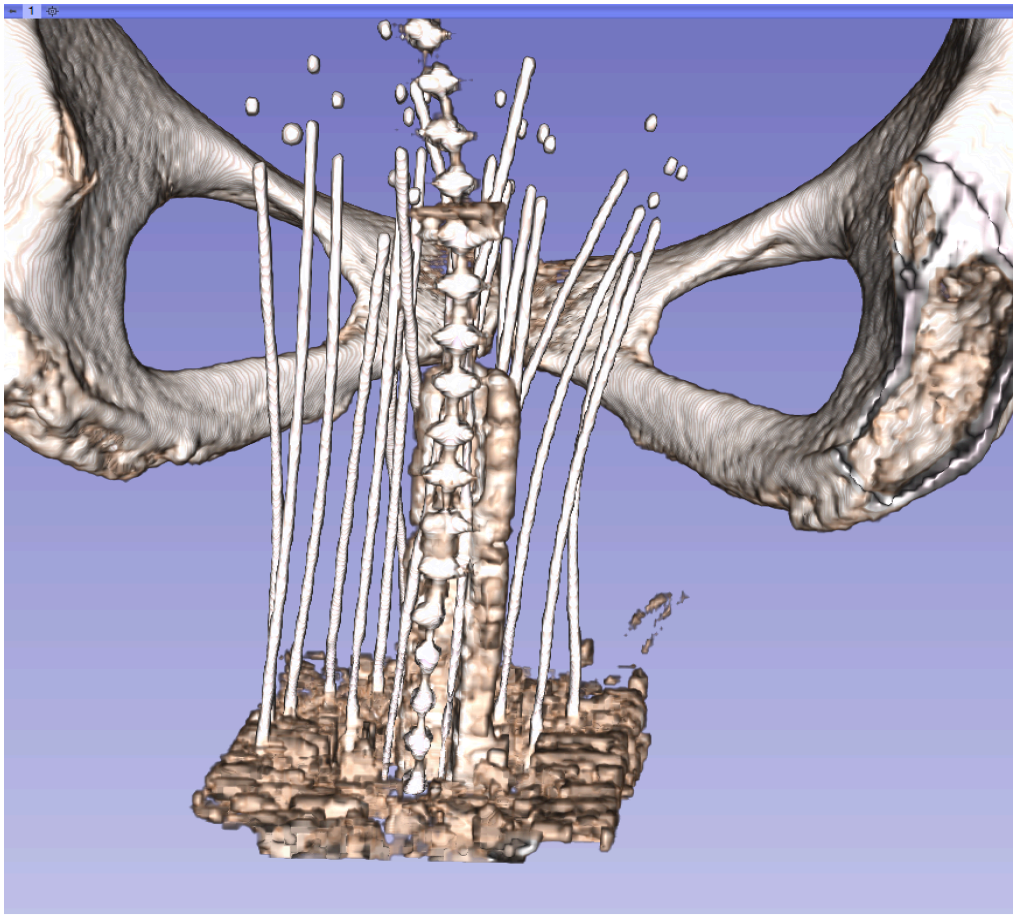

Fig. 7 Volume rendering of CT reconstruction. The needles on the right show curvature, which was given by the radiation oncologist in order to target the tumorous tissue avoiding the pelvic bones.

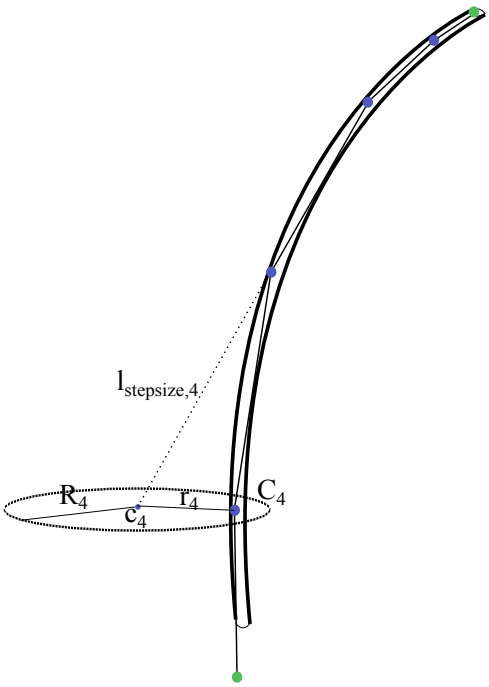

Fig. 8 Computation of the 4th control point

Starting with the needle tip, the algorithm looks for a direction maximizing the "needle likelihood" of a small segment in a conic region. The second extremity of this segment is saved as a control point, used later. Then, this step is iterated, replacing the needle tip by the latest control point. The height of the new conic region is increased as well as its base diameter and its normal is collinear to the previous computed segment. Five iterations give four control points, the fifth one being used as an extremity as well as the needle tip. From these four control points and two extremities a Bézier curve is computed, approximating the needle path.

A discrete formulation for this solution (or pseudo-code for this algorithm) is provided next.

Discrete Formulation of Algorithm

- Let $M \in \mathbb{N}$ and $M \geq 3$, be the number of iterative steps (control points).
- Let $n \in [1, \dots, M]$ be the n^{th} step of the segmentation process for one needle.

Once the first two control points are obtained, it is possible to estimate that the next one is going to be in cone defined by a certain solid angle. As far as the iteration goes and the number of control points adds up, the solid angle can decrease because the prediction gets better. Indeed the mechanical properties of the needle constrain its geometric trajectory. Trying to compute approximately the same number of operation at each step, the radius of the base of the cone is going to be approximately the same, but its height will increase. Thus the distance between to control points can be increased.

In order to have an algorithm following approximately the idea described above, the repartition of the control points follow the repartition of the M first Fibonacci numbers on a segment of the size of the needle length.

- Let $K_{lengthmin}, K_{radmin}, K_\theta, K_r, K_{seg}$ be constants defined by the user through the graphic user interface

  $K_{lengthmin}$ is the minimal difference between to control points along the Z-axis

  K_{radmin} is the minimal radius of the base of the cone

  K_θ is the minimal number of angle iterations

  K_r is the minimal difference between two radius iterations

  K_{seg} is the minimal number of evaluation points per segment

  These constants assure the robustness of the algorithm and avoid redundancy, as explained later.

- Let F_i be the Fibonacci's number:

$$F_0 = 0, F_1 = 1 \; and \; \forall n \geq 2, \qquad F_{n+1} = F_{n-1} + F_n \tag{7}$$

- Let h be the function of the repartition of the segment lengths, defined below

$$h(n,N) = \frac{\sum_0^n F_i - 1}{\sum_0^N F_j - 1} \quad \text{or} \quad h(n,N) = h(n-1,N) + \frac{F_n}{\sum_0^N F_j - 1} \tag{8}$$

- Let l_n be the length of the nth segment defined below

$$l_n = \max\left(h(n,M) * l_{needle}\, , K_{lengthmin}\right) \tag{9}$$

A comparison with a constant has been added to avoid to have too close control points in the first steps, which would result in computing several time the needle path for the same point (because of the discrete values of the pixel coordinates).

The same idea is used later to define R_n and R_{iter}.

- Let l_{needle} be the length of the needle. In particular l_{needle} has the following property (for $K_l = 0$)

$$l_{needle} = \sum_{n=1}^{M} l_n \tag{10}$$

- Let R_n be the radius of the base of the cone

$$R_n = \max\left(l_n \ , \ K_{radmin} \right) \tag{11}$$

- Let R_{iter} be the number of radius iterations

$$R_{iter} = \max\left(\frac{l_n}{2} + 5, K_r\right) \tag{12}$$

- Let θ_{iter} be the number of angle iterations and let N be the number of evaluation points per segment

$$\begin{cases} \theta_{iter} = K_\theta \\ N = K_{seg} \end{cases} \tag{13}$$

These parameters are currently constant, but can be optimized to depend on length of the step (l_n), thus to avoid to compute several times the calculation on a same path, in particular in the first step where N (the number of evaluation point per segment) can be greater than the number of slices between the extremity of the segment. It hasn't been done because it didn't seem necessary at this time (computation time lower than a second per needle).

- Let $\mathcal{R}$ be the list of the R_{iter} radius iteration values equally spaced from 0 to R_n, ϑ be the list of the θ_{iter} angles iteration values equally spaced form 0 to 2π.

$$\begin{cases} \mathcal{R} = \left\{ \frac{i}{R_{iter}} R_n \right\}, \text{ for } i \in [1..R_{iter}] \\ \vartheta = \left\{ \frac{i}{\theta_{iter}} 2\pi \right\}, \text{ for } i \in [1..\theta_{iter}] \end{cases} \tag{14}$$

- Let c_n be the center of the base of the previously designated cone.

$$c_{n+1:} \begin{pmatrix} \widetilde{x_{n+1}} \\ \widetilde{y_{n+1}} \\ \widetilde{z_{n+1}} \end{pmatrix} = \begin{pmatrix} x_n + (x_n - x_{n-1}) \\ y_n + (y_n - y_{n-1}) \\ z_n - l_n \end{pmatrix} \tag{15}$$

- Let E be the objective function defined below:

$$\begin{aligned} \mathrm{E}(r, \theta, N, x_0, y_0, z_0, x_1, y_1, z_1) \\ = \sum_{t=1}^{N} f_{pixel\ intensity} \left((1 - \frac{t}{N}) \begin{pmatrix} x_0 \\ y_0 \\ z_0 \end{pmatrix} \right. \\ \left. + \frac{t}{N} . \begin{pmatrix} x_1 + r.\cos(\theta) \\ y_1 + r.\sin(\theta) \\ z_1 \end{pmatrix} \right) \end{aligned} \tag{16}$$

$f_{pixel\ intensity}$ can be either: only the value of the pixel intensity at the coordinates given as input, or this value subtracted with the values of pixels in a delimited neighborhood. The second option adds gradient information to the segmentation process.

For magnetic resonance images, the needles appears dark on the images, thus the goal is to minimize the objective function E which means the value of the pixel on the path of the segment. An option is available to process images where needles appear bright (as in CT images for example), leading the algorithm to maximize the evaluative function.

- Let r_n (radius) and θ_n (angle) be the optimal parameters minimizing the objective function E:

$$(r_{n+1}, \theta_{n+1}) = \underset{\theta \in \vartheta \cup \{0\}, r \in \mathcal{R} \cup \{0\}}{\operatorname{argmin}} \mathrm{E}(r, \theta, N_n, x_n, y_n, z_n, \widetilde{x_{n+1}}, \widetilde{y_{n+1}}, \widetilde{z_{n+1}}) \tag{17}$$

- Let C_n be the control points, calcutated as below

$$C_{n+1}: \begin{pmatrix} x_{n+1} \\ y_{n+1} \\ z_{n+1} \end{pmatrix} = \begin{pmatrix} \widetilde{x_{n+1}} \\ \widetilde{y_{n+1}} \\ \widetilde{z_{n+1}} \end{pmatrix} + \begin{pmatrix} r_{n+1}.\cos(\theta_{n+1}) \\ r_{n+1}.\sin(\theta_{n+1}) \\ 0 \end{pmatrix} \tag{18}$$

Once the control points are obtained, an algorithm fits the control points with a Bézier curve.

- Bézier curve fitting

$$\mathrm{B(t)} = \sum_{k=0}^{n} \binom{n}{k} (1-t)^{n-k} t^{k} \mathrm{C_k}, \qquad t \in [0,1] \tag{19}$$

$n+1$ control points define a n^{th} degree Bézier curve as a linear combination of Bernstein basis polynomial. The first and last control points define the extremity of the curve. The interior points pull the curve toward them.

3.2 Applicator Registration

In this section, novel post-processing methods are described for rapid localization of the brachytherapy applicator in MRI. In particular, methods are described for localization of the Syed-Neblett interstitial applicator, which is typically used for the most complex insertions. This applicator consists of a rectangular template that contains holes through which needles are positioned, and a cylindrical obturator that holds the template and needles in place.

Fig. 9 Applicator: template (blue), obturator (white) and needles (gray).

The key steps of this applicator registration method are as follows. The method first uses geometrically salient landmarks to obtain an initial registration. This registration is then used to define a region of interest in which simple image processing techniques are used to segment the template and the obturator. The dense set of points that comprise the surfaces of the template and the obturator are then used to refine the initial registration and hence obtain the final registration result.

Landmark-based Registration

Artificial landmarks are created using a set of four vitamin E capsules (approximately cylindrical in shape with 6 mm diameter and 15 mm length) that are placed in the four corners of the template. Vitamin E appears bright in MR images, which facilitates the detection of these markers using an algorithm that is customized to search for bright circles of diameter 6 mm (in MR cross-sections) in a pre-specified configuration. The figure below illustrates the four corners of the template in which the vitamin E markers are placed.

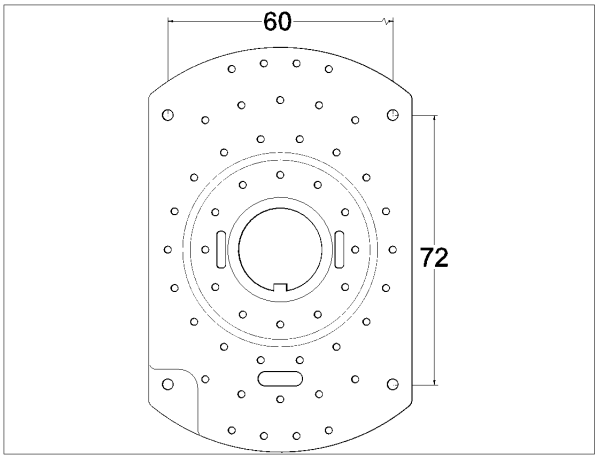

Fig. 10 2D view of the template, part of the gynecological applicator for brachytherapy.

As described in Chapter 2 (Prior Work), the Hough transform is a feature extraction technique which first was applied to the identification of straight lines in images and then was extended to detect arbitrary shapes, most commonly circles and ellipses and was renamed "Generalized Hough Transform" (GHT) [4,5]. In this work, an open source implementation [ref *itkHoughTransformRadialVotingToImageFilter*] of the Circle Hough Transform (CHT) [7] was used.

Once the CHT is performed, the following algorithm is used to filter and sort the circles. The input to this algorithm is a set of centers of the detected circles and their radii, and the output is a sorted list of 4 centers of circles that are 6 mm in diameter, and in the correct geometric configuration.

Algorithm Filtering and Sorting the Circles

- Let u be equal as approximately the distance between opposite corners on the small side of the template (60 mm).
- Let v be equal as approximately the distance between opposite corners on the long side of the template (72 mm).
- Let w be equal as approximately the distance between opposite corners on the diagonal of the template (93.8 mm).
- Let $\{C_1, \dots, C_n\}$ be the centers of the detected circles where n is the number of detected circles with the right radius.
- Let (U_i, V_i, W_i) be defined as following: U_i the number of centers distant from C_i from u, V_i the number of centers distant from C_i from v, W_i the number of centers distant from C_i from w.

1. $\forall i \in [1..n]$, if $U_i + V_i + W_i \geq 3$, add C_i to the list $L_{valid\ circles}$.
2. Remove duplicates (same circle being detecting one slice above or below)
3. Order the list $L_{valid\ circles}$ to have the similar configuration as shown in Fig. 11.

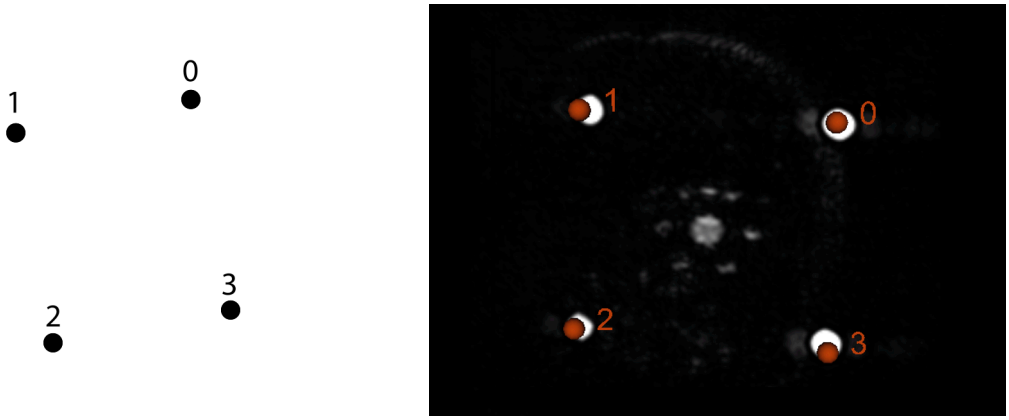

Fig. 11 Labeling of the detected circles. On the left, drawing of the labeling for a template in a vertical position; on the right, results of the CHT in a 3D view in 3D Slicer: fiducials markers overlaying an axial view, template in horizontal position.

From computing the distance of each of the four detected circles with all others, and adding the information of their relative position, the algorithm identifies them to their specific corresponding landmark on the template CAD model, thus creates an ordered fiducial list of four fixed points ("fixed landmarks"). Then, the corresponding points of the CAD model ("moving landmarks") are registered against the fixed landmarks, using a point-based registration method [21].

Fig. 12 Outcomes of the first registration. On the left, the axial view; on the right, the sagittal view. We can observe the misplacement of the applicator through the cross-sections of the obturator (light-blue) and the template (blue).

Although fast and robust, this registration needs improvement. All four landmarks are contained in the same plan and are relatively close to each other. A small error of registration can become dramatically prominent as the distance to these landmarks increases. For example with an error of only 1° in x-axis or y-axis (z-axis being the obturator axis, the origin being the intersection of the z-axis and the center of the template), for a 170 mm needle situated in the center of the obturator, the target error at the tip is already $170 * tan(1) \approx 3mm$. In order to improve the registration, a fifth landmark situated at the tip of the obturator could have help to reduce the target error. For feasibility reasons, this solution has not been pursued. However adding information of obturator has proven to be satisfying.

Point-cloud based Registration

Using the landmark registration as its initialization, the point-cloud based registration is performed as follows:

- First, segments points on the template by using dynamic thresholding on a region of interest outlining the template;
- Second, segments points on the obturator by noise-filtering on a region-of-interest outlining the obturator, thresholding, followed by selection of the largest "dark" continuous area (as plastic material appears dark on MR images);
- Third, registers the point-clouds obtained in the first two steps, against the one extracted from the CAD models surfaces. It uses the *iterative closest point registration* (ICP) [16] which is a robust technique to register free form surfaces with high precision, details of which are provided in the previous chapter (Prior Work).

3.3 Software Development

Workflow Description

iGyne is currently articulated in seven steps: 1) procedure selection, 2) applicator selection, 3) data importation, 4) initial applicator registration, 5) refined applicator registration, 6) needle position planning, 7) needle detection. The graphic user interface (GUI) offers an option to jump directly to the needle detection step, without having to register the applicator first, in which case the user can still process the registration later in order to take advantage of the labeling feature.

Fig. 13 presents the usual workflow of the use of iGyne as part of the interstitial brachytherapy treatment workflow. The first scan differentiates itself from the one of the following scans because of the addition of the applicator registration part. However, the registration can also happen later if, for some reasons (template with landmarks not covered by the MRI), it is not accomplished after the acquisition of the first axial MR scan.

Fig. 14 introduces a more detailed workflow diagram of iGyne. It shows the process followed by the radiation oncologist to optimally insert the needles in order to cover the most of the tumorous tissue/ to avoid the most as possible the organs at risk. This operation is a trial-and-error process and identifying which needles need readjustment is of critical importance.

The integration of the radiation treatment (RT) planning is possible with the Slicer RT module for 3D Slicer which allows to import/export and visualize RT data.

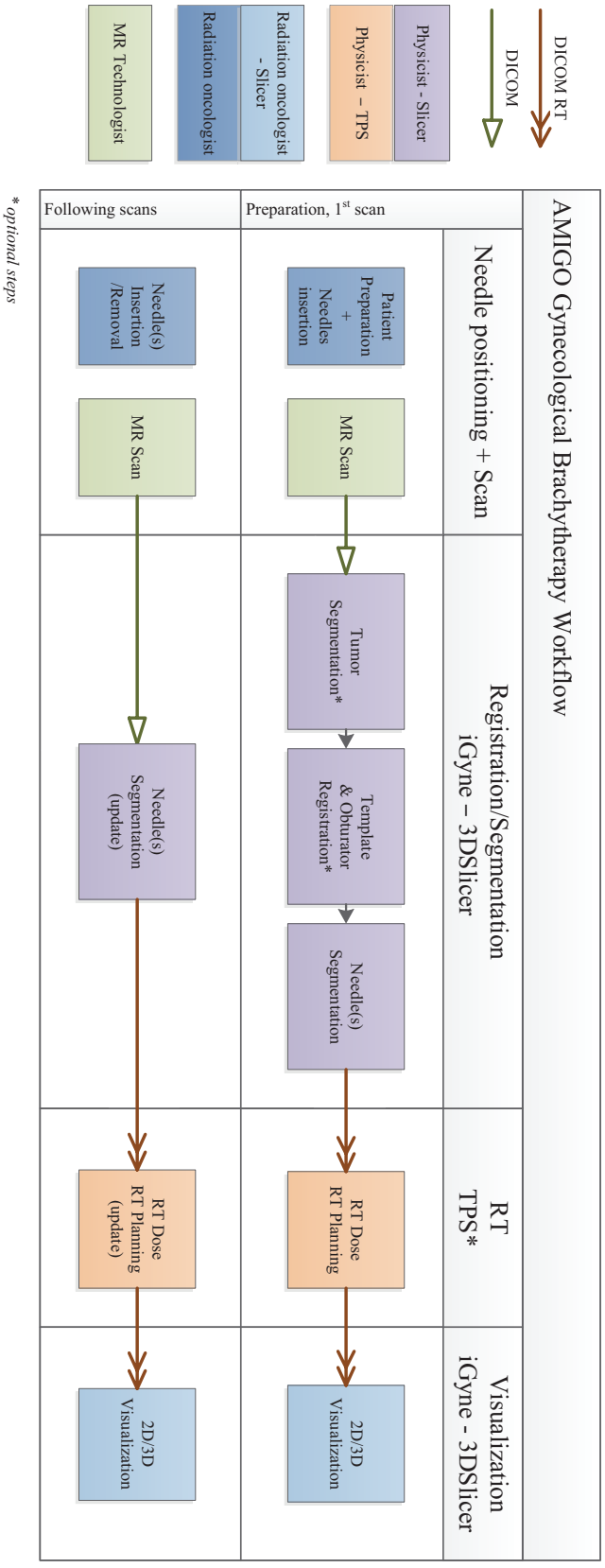

Fig. 13 Overview of iGyne as part of the AMIGO gynecological brachytherapy workflow.

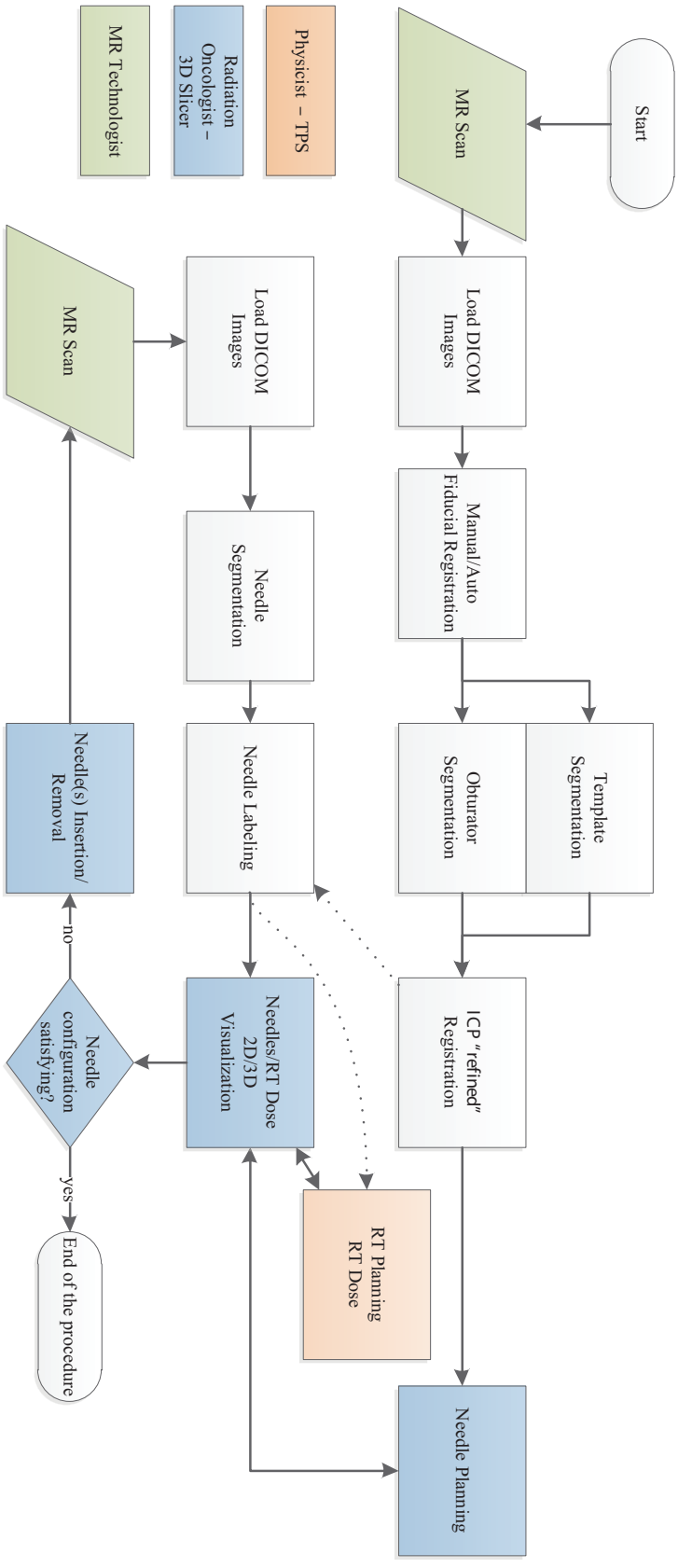

Fig. 14 Detailed workflow of iGyne as part of the AMIGO gynecological brachytherapy workflow.

As the interstitial brachytherapy workflow, which requires experience from people from different field, iGyne interfaces with them. Fig. 15 shows the repartition of the interactions with iGyne: The MR technologist is responsible for providing MRI datasets acquired with the right MR sequence (axial 3D-b-SSFP), thus that can be processed by iGyne, and one of the MRI obtained during the case has to contain the template and its bright fiducial markers. A physicist can export the extracted needle from Slicer through the Slicer RT module, update the treatment planning in a Treatment Planning Software (TPS) like Eclipse, and load it back to Slicer to provide the visualization to the radiation oncologist. The latter can "play" with the axial, sagittal, coronal and 3D views and disposes of features of iGyne allowing to reformat the sagittal view in a plane contained most of the observed needle (or all of it in case of a straight needle).

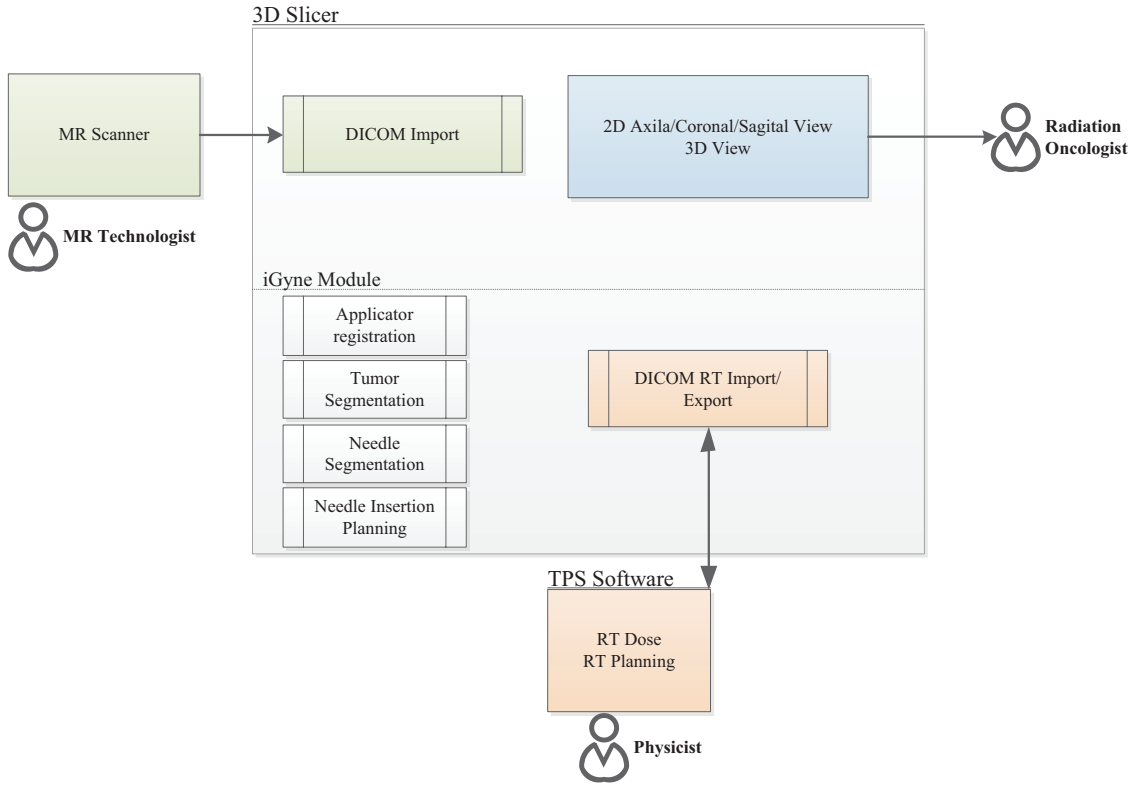

Fig. 15 iGyne user-diagram. Roles and interactions of the MR Technologist, radiation oncologist and physicist around 3D Slicer and iGyne.

To provide the right amount of options and features at the right time, iGyne is articulated in seven steps described below, each step answering a specific task. However, the flow of the computed data should be able to navigate between the different steps, allowing this way the transfer of needed information. Fig. 16 introduces the class diagram of iGyne, which shows the architecture of the module and the connections between the different steps.

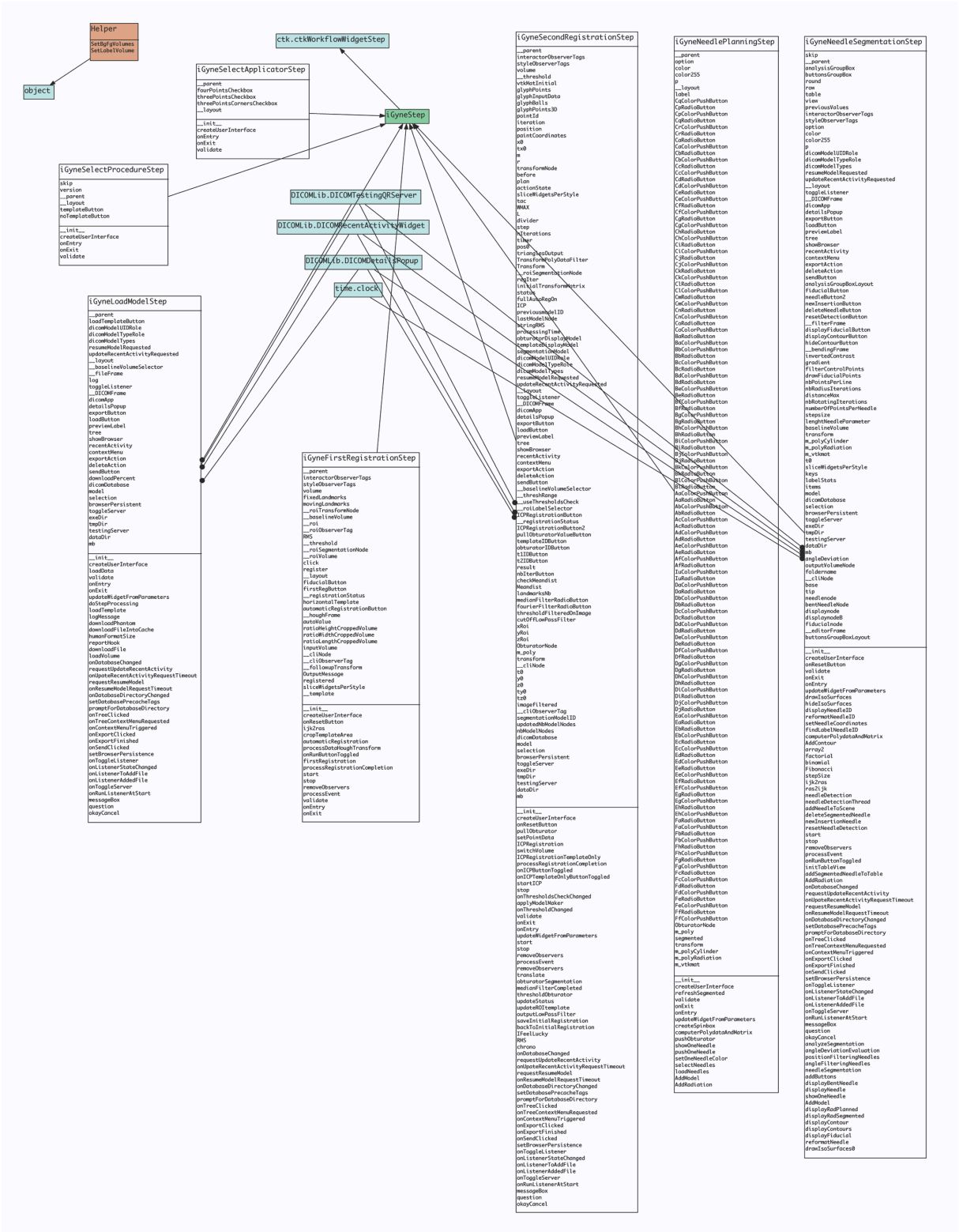

Fig. 16 iGyne class diagram generated by pyNsource. The seven classes (*iGyneSelectProcedureStep, iGyneSelectApplicatorStep, iGyneLoadModelStep, iGyneFirstRegistrationStep, iGyneSecondRegistrationStep, iGyneNeedlePlanningStep* and *iGyneNeedleSegmentationStep*) are part of the *iGyneStep* class through which they can exchange data and which is constructed form the *ctkWorkflowWidgetStep* class. The DICOM classes are accessed from three of the iGyne steps (*iGyneLoadModelStep*, *iGyneSecondRegistrationStep* and *iGyneNeedlePlanningStep*

Procedure Selection

The procedure selection step is made to offer the user the possibility to choose different procedures with preloaded parameters for the following step. Currently, only two choices are available: select the presence of a template or not. If not, the user is directly driven to step 7.

Applicator Selection

In the applicator selection step, the user is able to precise the applicator used for the case. Depending on the choice, a scene is loaded containing several CAD models of the applicator parts as well as a fiducial list. On old cases the user had to choose manually a set of 3 points corresponding of the positions of Vitamin E capsules situated in the notches of the template. On newer cases, the Vitamin E capsules are placed at the corners of the template and the registration is fully automated. Thus, this step gives a retro-compatibility with older cases. It is also ready to add new applicator choices, to expand the domain of application of iGyne.

Data Import

The role of the data import step is to enable iGyne to communicate with MR scanners through the standard DICOM protocol. The MR technologist sets the scanner console to push automatically new scans to the client where iGyne is installed. In a timeframe of thirty seconds to one minute, the DICOM data are converted to a scalar volume and loaded to the scene. The option to load data directly from NRRD files is also available, allowing the user to work off-case.

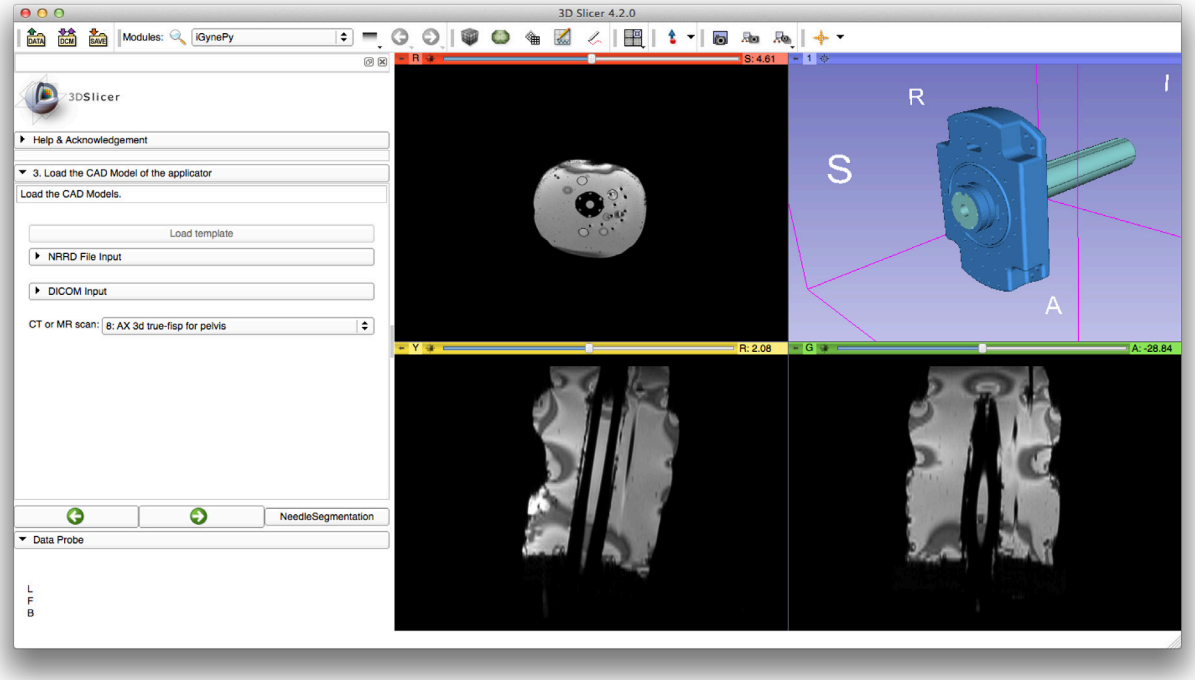

Fig. 17 Data loaded to the scene with an axial view (upper left), a sagittal view (lower left), a 3D view and a coronal view (lower right).

Initial Registration

Once all the elements of the scene are loaded, it is time to start the registration. A first initial registration step is required as described in section 3.2. Currently, no user input is asked as the detection of fiducial points is automated. However, to allow working on older cases or in case of an unsatisfying detection, the user can click directly on the landmarks, 3 or 4, depending on the choice he previously made in the step "applicator selection". Once the right number of landmarks is acquired, the landmark registration is computed in less than a second. If the result is satisfying, the user can go to the next step, otherwise, and adjustment of the fiducial is possible the registration can be recomputed. Below Fig. 18 presents common results obtained after the first initial registration.

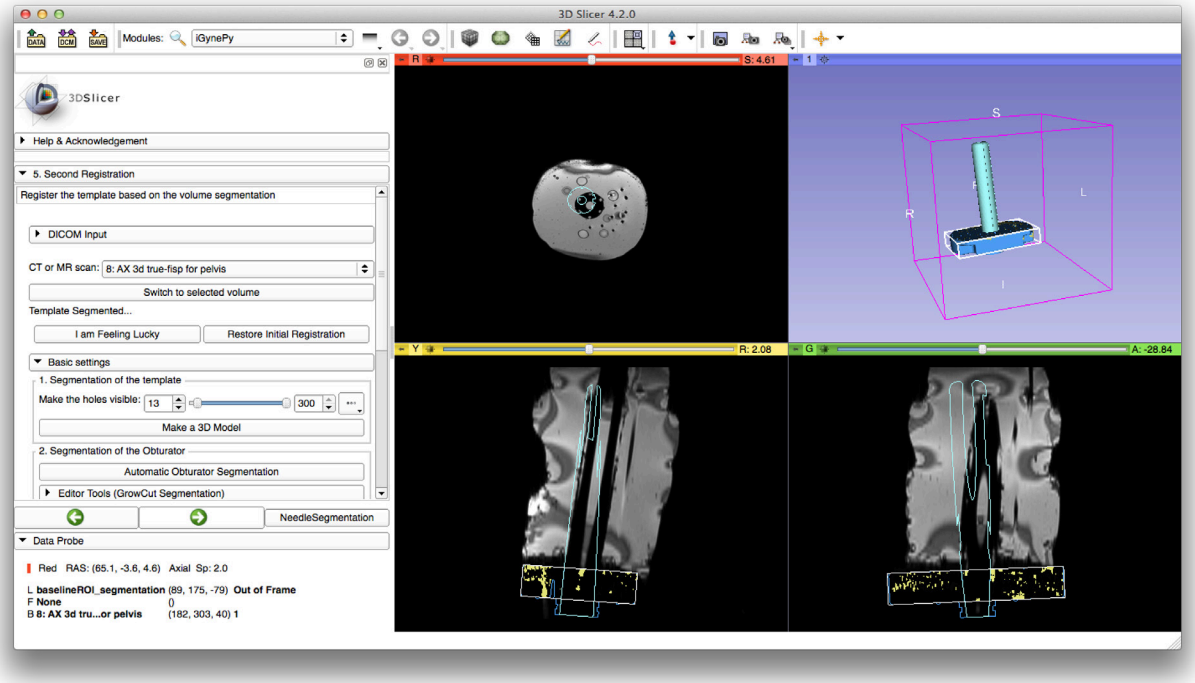

Fig. 18 Results of the initial registration, before the refined registration.

Refined Registration

The refined applicator registration step offers fully automated computation to complete manual parameterization if needed. Thus, several segmentation methods are available to segment the obturator, and the registration parameters can be tweaked. Among these segmentation methods there are:

- Interactive GrowCut segmentation [22]: through the embedded editor module, the user applies with rough gesture two different labels inside and outside the volume to segment. In about thirty seconds to two minutes (depending on the amount of initial information given) a label defines the volume and can be then converted to a model though the "model maker" feature available from the embedded editor module.
- Noise filtering with a low-pass filter followed by low-level heuristics: The parameters of the low-pass filter applied in the frequency domain are modifiable, as well as the dynamic value of the threshold, used to select the largest continuous dark area. This method has a computation time of an average of five seconds.

- Noise filtering with a median filter followed by low-level heuristics: the geometry of the median filter can be modified. This method gives currently the best compromise between computation time, and results and don't need any user input. Thus it is selected by default

By default, the most efficient parameters are chosen and all steps of the refined registration are computed successively after a click on the "I am feeling luck" button that can be seen in Fig. 19.

Evaluation functions have also been integrated to allow developers to measure time and accuracy of the chosen methods and parameters. Beside the control interface, 2D views display cross sections of the applicator in axial, sagittal and coronal planes giving the user a visual characterization of the registration state.

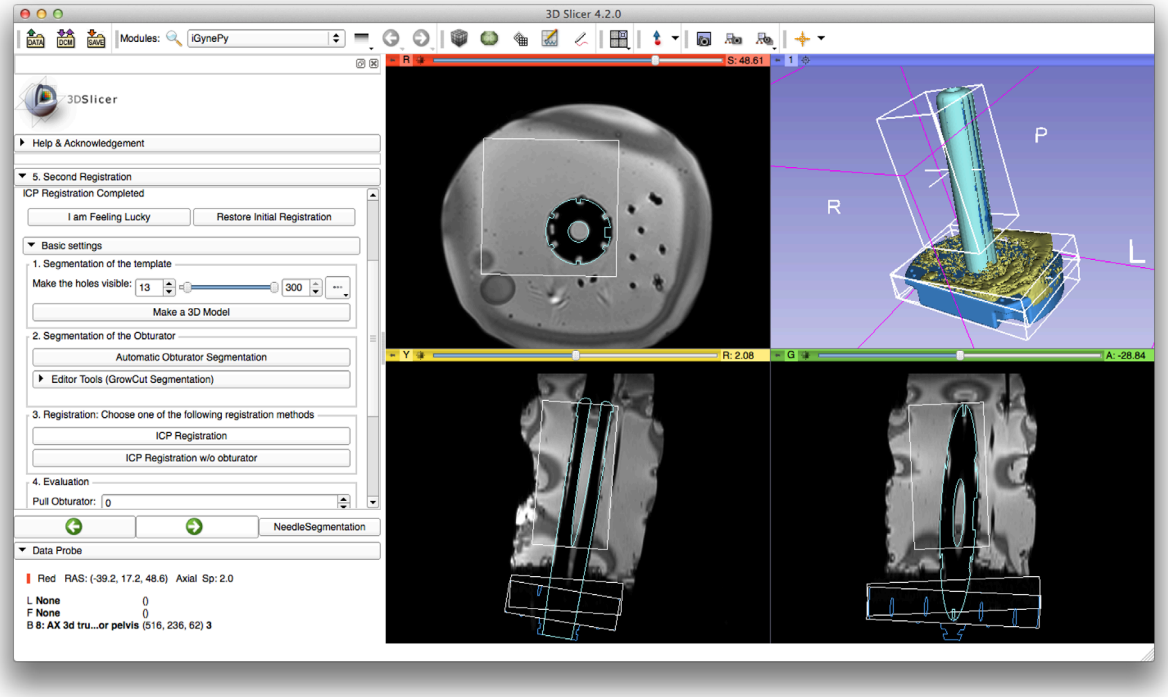

Fig. 19 Refined registration results. We can observe the cropping box (in white) outlining the obturator and the template in its initial position (after the landmarks registration).

Needle Insertion Planning

The applicator registered, the radiation oncologist can go to the needle-planning step, to insert virtual needles and visualize their approximate trajectory. The approximation comes mainly from the assumption that the deflection is not anticipated and currently only straight needles are drawn. As partially shown in Fig. 20, a map represents the sixty-three holes of the template where a needle can be inserted and clicking on them will display/hide the respective needle and its label. The length of the needle can be adjusted and position-depending color-coding gives an easy way to distinguish needles from each other. If during the next step, needles have been detected, a red square will outline the label of the detected needle on the needle map. Because during a case several scans are made at different time points, the last inserted and detected needles benefit from a perceptible distinct color coding to another level of information to the radiation oncologist, operating sometime with more than 30 needles.

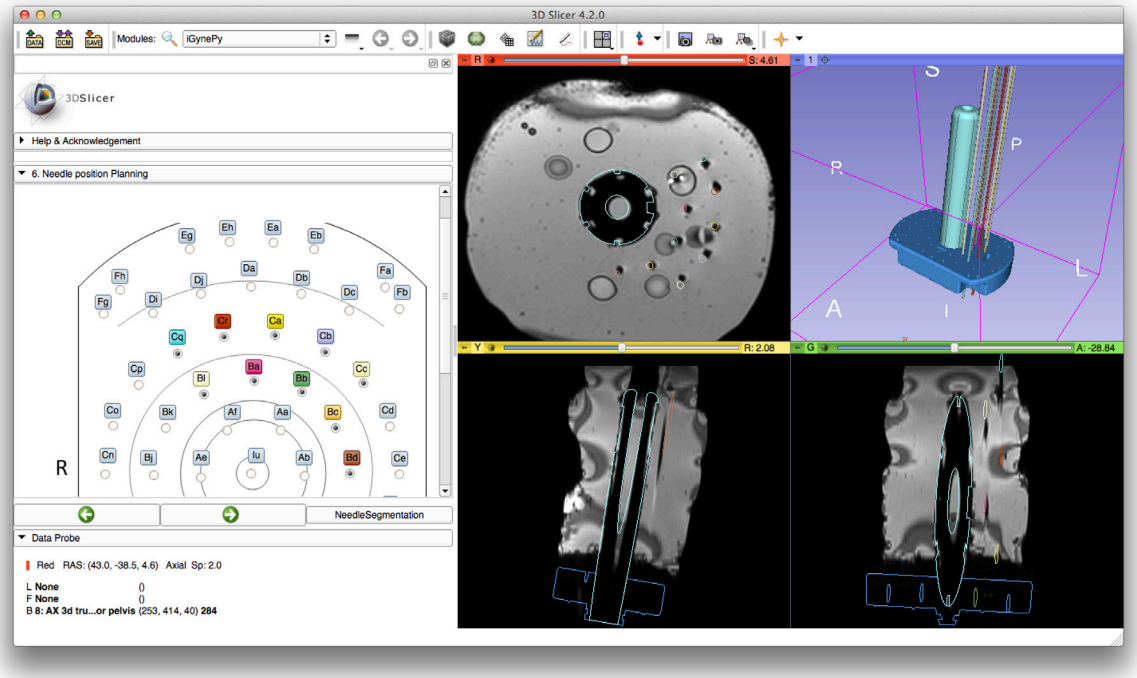

Fig. 20 Needle-planning step: On the right, 2D and 3D views of the models of the virtual needles. Even if the registration looks right, of the applicator looks right, it is possible to observe the "target-error" of these planned needles, especially on the axial view (red slice). On the left, GUI letting the user insert virtual needles. Arbitrary colors have been chose for each of them.

Needle Segmentation

The needle segmentation step is the keystone of iGyne. By clicking on the tips of the needles the user gives the algorithm the needed input to start the needle segmentation (c.f. section 3.1.3). In less than a second, the extracted needle is rendered in 3D and the cross sections of the needles are displayed in the 2D axial, sagittal and coronal views. For each detected needle, buttons are generated to let the user display or hide a needle, or reformat the sagittal view to a plane containing a needle or most of it in case of a bent needle. A table summing up the properties of the detected needles is displayed as well, as shown in Fig. 21.

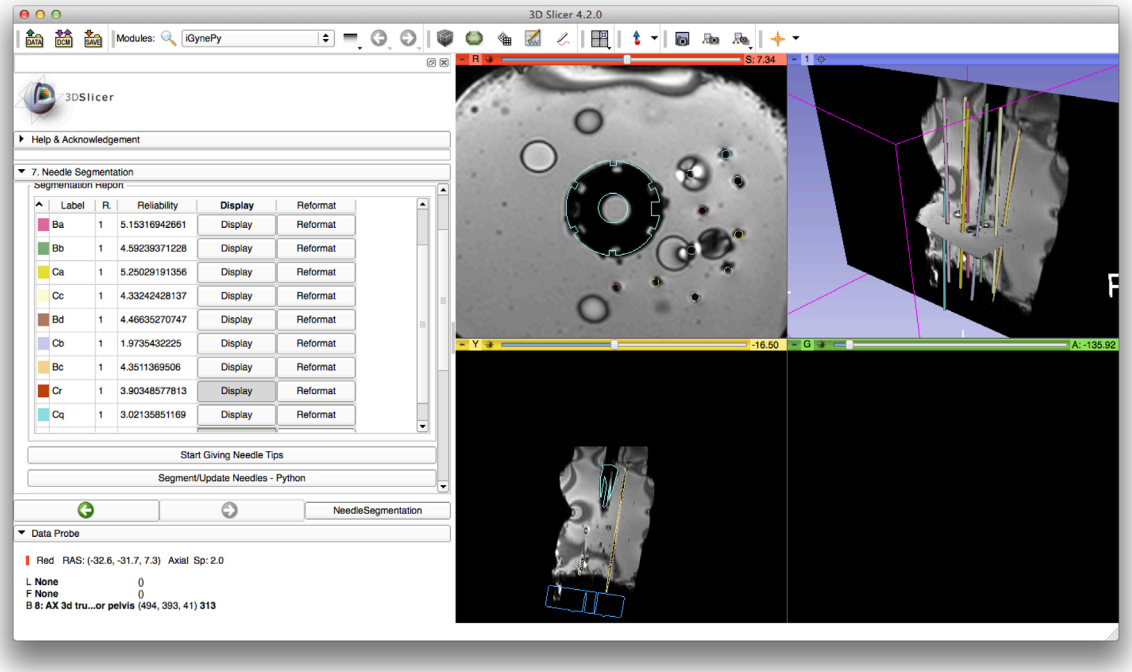

Fig. 21 Needle segmentation step. The red slice and the yellow slice show the cross-sections of the segmented needles. The 3D view offers an overview of the models of the segmented needle. On the left side of the GUI displays a part of the interface allowing the user to manage the segmented needles and to reformat the sagittal view.

Another feature, presented in Fig. 22, offers to display iso-contours and iso-surfaces, giving an approximate overview of the cold-zones and hot-zones. A cold-zone is a zone lacking of needles, whereas a hot-zone is a zone where enough needles have already been inserted.

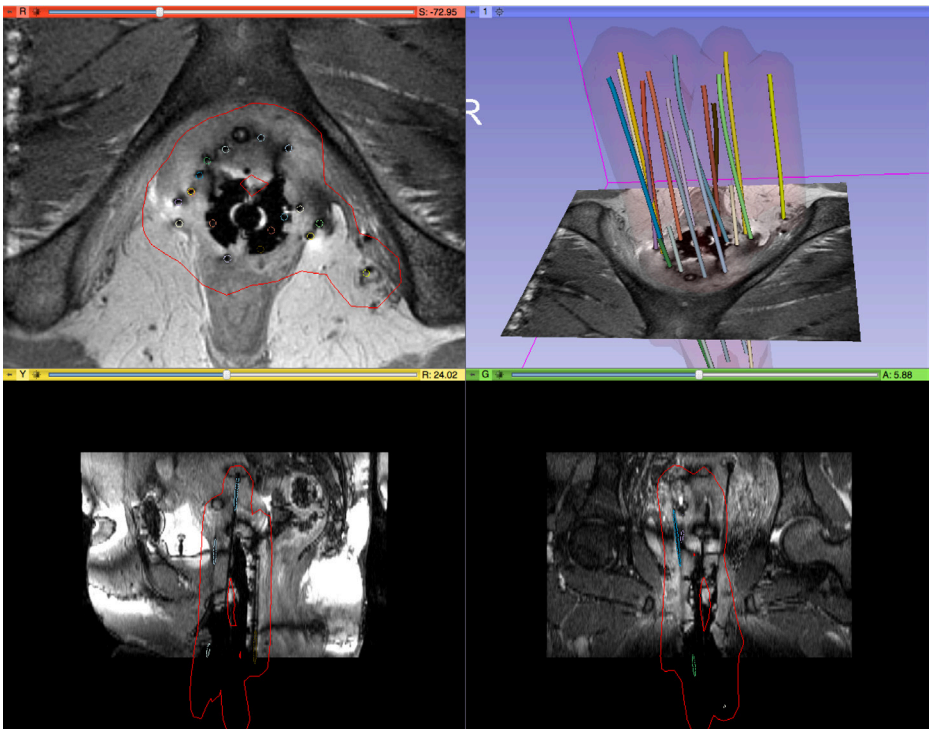

Fig. 22 Iso-surfaces and iso-contours representing all points distant of 10mm from the closest needle.

If an applicator has been previously registered, an algorithm determines the closest holes through which the needle has been inserted and propagates its label and its color property to the segmented needle. If it happens that two needles have been given the same label, only the longest one is kept. This feature allows the user to give several tip positions for a needle while browsing through the slices. For each needle, the vector direction of its linear approximation is compared to the direction of the virtual needles and the angular deviation is computed. Thus, it gives the user the possibility to identify and remove needles having strong angular deviation value. This option is not checked by default because sometimes the radiation oncologist needs to insert needles in uncommon directions.

4 Results and Discussion

In this chapter we present results of using the iGyne software first on MR data of a phantom, and then on ten patients MRI.

4.1 Phantom Experiments

4.1.1 Phantom Description

In order to design and evaluate the algorithms presented in this thesis, a phantom was made from commercially available transparent gel wax, made from heterophase thermally reversible hydrocarbon oil gel based on thermoplastic rubbers, as described by Morrison and Heilman in a 1997 patent [23]. The choice of this material was motivated by the following advantages:

- High magnetic resonance sensitivity, which leads to better images
- Viscosity low enough to allow easy insertion/manipulation of gynecological obturator and needles, and high enough to maintain the configuration of the different elements parts of the phantom and allow for reproducible experiments.
- High optical clarity, which allows ease in controlling the configuration of the different elements of the phantom. Indeed, this polymer retains its amorphous characteristics below its glass transition temperature T_g.
- Reusable by simple melting, because of its thermal reversibility.
- Price and commercial availability.

The construction of the phantom involves several steps. In each step, a small portion of wax is melted in an oven at 300F (above its melting point T_m) and then poured in a transparent plastic container. Small marbles ("*Magic Marbles*"), with different MR sensitivity, were added to the layer of wax while it was still in a liquid state (between T_g and T_m). Once the wax cooled down sufficiently (below its glass transition temperature T_g) and becomes fixed, a new layer was added following the same process. These steps were repeated until the container was filled to the desired level. During each step, the position of the obturator from the gynecological applicator was maintained in the center of the plastic container. At the end, the Syed-Neblett template was placed and 10 gynecological MR compatible needles (tungsten, 2 mm diameter) were inserted. The resulting phantom is illustrated in Fig. 23.

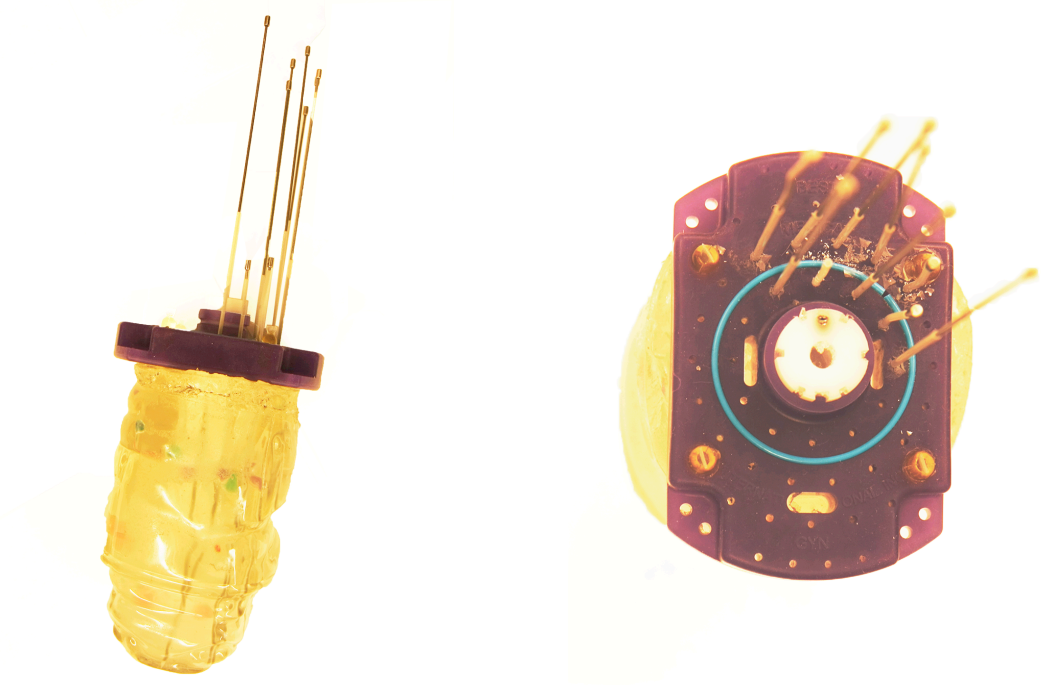

Fig. 23 Phantom created from gel wax. The left picture shows the needles, the template, as well as the colored marbles. The picture on the right shows a different view from which the template (purple) and the obturator (white) are clearly visible, along with MR-visible vitamin E filled markers positioned in the corners of the template.

4.1.2 **Experiment**

This phantom was imaged in the AMIGO suite of the Brigham and Women's Hospital with a Siemens 3 Tesla Verio wide bore (70cm) MR scanner. 3D AX b-SFFP and 3D AX SPACE TRIAL imaging sequences were used, which are the same as the ones used clinically during interstitial gynecological brachytherapy procedures.

The result of needle extraction developed in this thesis was compared to segmentations performed manually by a physician with experience in segmentation of gynecological MRI datasets.

The experiment was performed twice to assure reproducibility.

4.1.3 **Needle Segmentation Evaluation**

Visual Inspection

In this section, pictures of the results of the needle segmentation for the first experiment are presented for visual inspection by the reader. It is possible to estimate the error between the manual segmentation and curved needle segmentation by superimposing the results of both segmentations. It should be noted that for each needle comparison, there is less than a "needle-diameter" of error, because models from both segmentations always overlap. Similar results were obtained from the second experiment, and are therefore omitted.

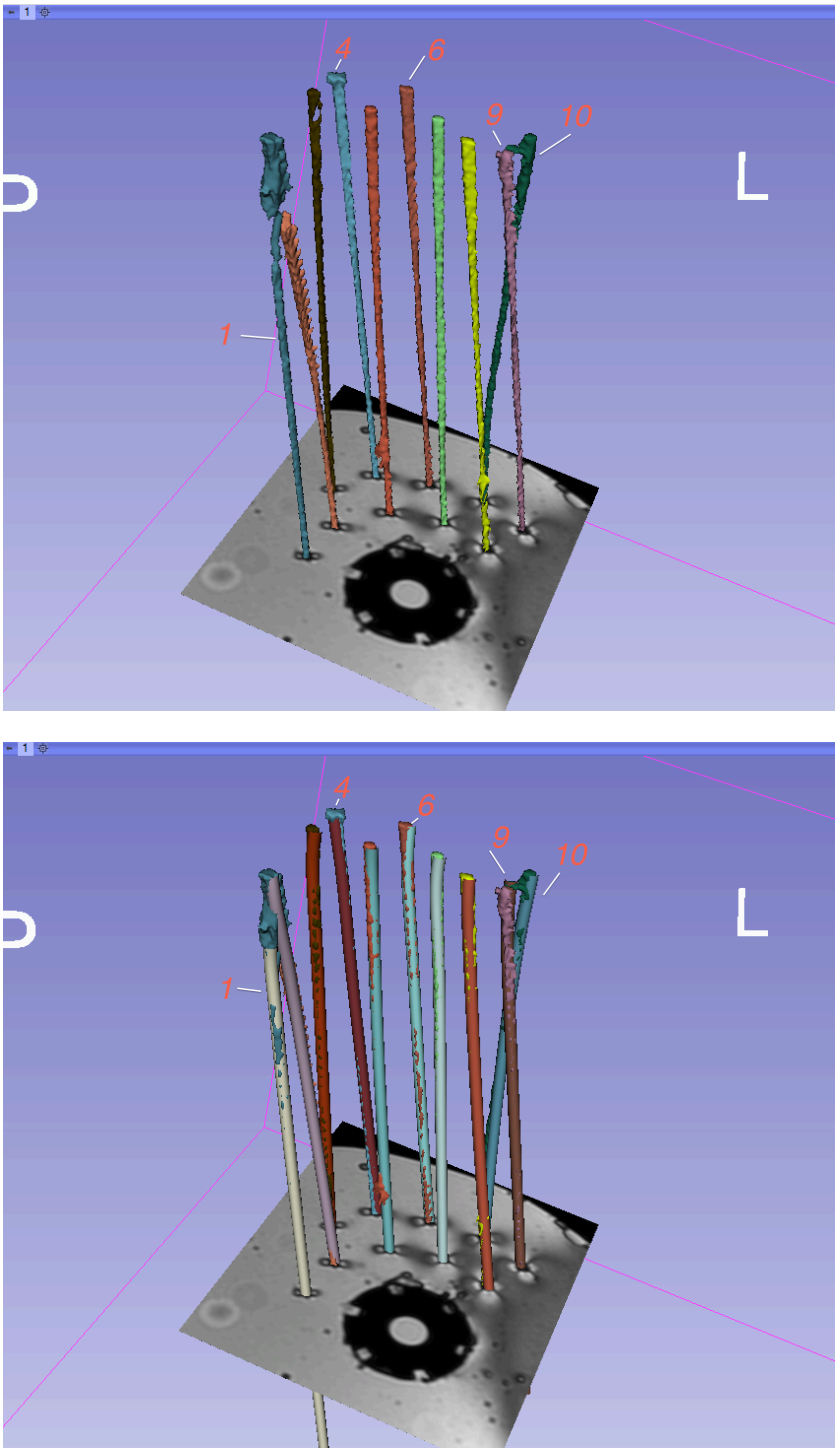

Fig. 24 Top: results of the manual segmentation done by an expert. Bottom: results of the curved needles extraction superimposed with the manual segmented needle. Different colors have been chosen to emphasize the differences between both segmentations, as on needle 1, 4, 6. Needles 9 and 10 illustrate the ability of the algorithm to correctly detect crossing needles.

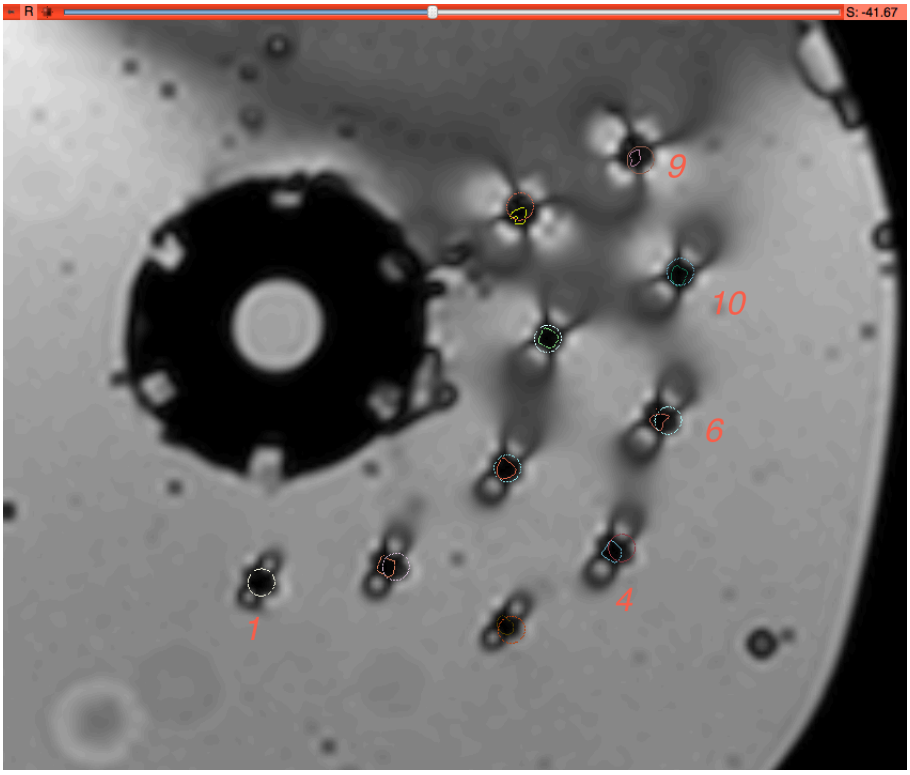

Fig. 25 Axial view and cross-sections of both manually and algorithmically segmented needles. The more irregular cross-section are from the manual segmentation which is to be expected given the difficulty of the task.

Quantitative

The accuracy of the segmentation algorithm was compared to manual segmentation of the needles. The metric used to quantity the accuracy of the needle segmentation is the Hausdorff distance (HD) [24], defined below:

$$d_H(X,Y) = \max\{\sup_{x\in X}\inf_{y\in Y} d(x,y),\ \sup_{y\in Y}\inf_{x\in X} d(x,y)\}$$

where X and Y are two non-empty sets of a metric space (M,d), sup represents the supremum and inf the infimum.

In words, the Hausdorff distance is a symmetric metric, that reports the distance between closest points from each point cloud, that disagree the most.

The needle extraction accuracy was also quantified by measuring the standard deviation between the distance of closest points of each point sets:

$$Z = \{\sup_{x\in X}\inf_{y\in Y} d(x,y),\ \sup_{y\in Y}\inf_{x\in X} d(x,y)\}$$

$$\sigma(Z) = \sqrt{E\left[\left(Z - E(Z)\right)^2\right]}$$

It should be noted that the lowest point of the manual segmentation of each needle lies on surface of the template, while the lowest point of each algorithmically segmented needle

depends on the needle length parameter provided in its settings. As a result of this, the length of the corresponding (manual vs. algorithmically segmented) needles may differ. Therefore, prior to the computation of the Hausdorff distance, the needles where truncated at the base, to compare pairs of manually and automatically segmented needles having the same length.

Table 1: Hausdorff distance results for experiment 1. In column 2, Hausdorff distance between manually segmented needles and extracted curved needles. In column 3, standard deviation between manually segmented needles and extracted curved needles. The unit is millimeter.

Needle number	**Hausdorff distance (mm)**	**Standard deviation (mm)**
1	1.75	0.29
2	1.63	0.28
3	1.83	0.32
4	2.14	0.32
5	1.53	0.27
6	2.39	0.31
7	3.82	0.56
8	1.60	0.25
9	1.98	0.33
10	3.21	0.35

Table 2: Hausdorff distance results for experiment 2. In column 2, Hausdorff distance between manually segmented needles and extracted curved needles. In column 3, standard deviation between manually segmented needles and extracted curved needles. The unit is millimeter.

Needle number	Hausdorff distance	Standard deviation
1	1.78	0.28
2	1.59	0.30
3	2.07	0.34
4	2.10	0.34
5	1.72	0.27
6	2.22	0.30
7	1.51	0.27
8	2.09	0.28
9	1.52	0.25
10	2.61	0.35

The Hausdorff distance is computed by calculating the distance described above, between the point clouds composing the extracted needles.

From both experiments, it can be seen that values of the Hausdorff distance are in range of 2-3 mm. However, from the pictorial evaluation, lower values – less than a needle-diameter, which is 2 mm – were expected. After investigation, it was found that the additional error is due to the irregular repartition of the points used in the construction of the model representing the algorithmically segmented needle (constructed with the VTK class *vtkTubeFilter*). Furthermore, the MRI used presents an axial spacing of 2 mm, which leads to another error in the construction of the manual segmented needle. Finally, the manual segmentation is a particularly difficult task, which cannot be sub-millimeter accurate.

For both experiments, the computation of the standard deviation defined above gives low values, which reassure the quality of the curved needle segmentation.

4.2 Results on Patient MRI

4.2.1 **Experiment**

The MRI datasets used in this section where acquired during gynecological interstitial brachytherapy cases performed at the AMIGO suite of the Brigham & Women's Hospital between June 2012 and December 2102. The scanner used is a Siemens 3 Tesla Verio wide bore (70 cm) MR scanner. 3D AX b-SFFP and 3D AX SPACE TRIAL imaging sequences were used, which are the usual ones used clinically during interstitial gynecological brachytherapy procedures.

The methodology of the evaluation is the same as followed in section 4.1.3.

4.2.2 **Needle Segmentation**

Case 1

Table 3: Hausdorff distance results for case 1. In column 2, Hausdorff distance between manually segmented needles and extracted curved needles. In column 3, standard deviation between manually segmented needles and extracted curved needles. The unit is millimeter.

Needle number	Hausdorff distance	Standard deviation
1	2.49	0.38
2	2.81	0.46
3	2.45	0.48
4	3.28	0.51
5	2.35	0.40
6	2.43	0.46
7	2.34	0.47
8	2.01	0.38
9	2.30	0.40
10	4.45	0.69

Discussion:

The values of HD for case 1, as shown in the table above, are consistent with what was expected, except in the case of needle 10 which shows a 4.45 mm HD error. The cause for this error can be understood as follow. The physician doing the manual segmentation proceeds slice by slice, and it may be difficult to estimate the trajectory of a needle, particularly when it enters a dark area. Thus the manual segmentation may sometimes be inaccurate. However, the algorithm used for the needle extraction use the previously detected points to estimate the position of the following ones, which can result in a better accuracy compared to the manual segmentation, as for the needle 10.

The Fig. 26 On the left and the middle, comparison of the 3D models of the manually and automatically segmented needles. On the right, cross-sections of the needles in an axial view close to their base. After investigation, it seems that the result of the algorithm is closer to the reality than the manual segmentation.Fig. 26 illustrates this needle – on the left is shown the manual segmentation, in the middle is shown an overlay of the algorithm results (yellow) on the manual segmentation, and on the right is an axial cross-section of the MRI taken at the level where the disagreement (which results in 4.45 mm HD) occurs.

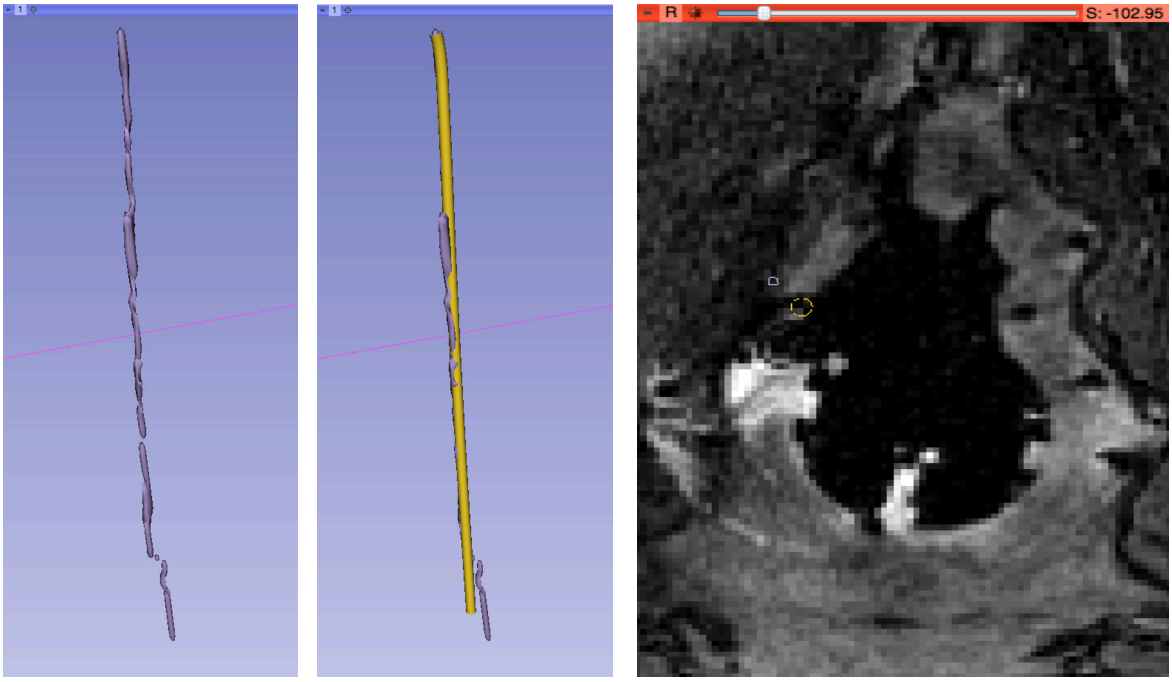

Fig. 26 On the left and the middle, comparison of the 3D models of the manually and automatically segmented needles. On the right, cross-sections of the needles in an axial view close to their base. After investigation, it seems that the result of the algorithm is closer to the reality than the manual segmentation.

Case 2

Table 4: Hausdorff distance results for the case 2. In column 2, Hausdorff distance between manually segmented needles and extracted curved needles. In column 3, standard deviation between manually segmented needles and extracted curved needles. The unit is millimeter.

Needle number	Hausdorff distance	Standard deviation
1	3.09	0.50
2	4.09	0.58
3	3.66	0.69
4	2.69	0.50
5	5.75	0.92
6	5.20	1.31
7	3.93	0.63
8	5.13	0.64
9	2.18	0.41
10	3.49	0.53

Discussion:

The unusual low quality of the MRI datasets makes that the results obtained may be considered mediocre for needle 5,6 and 8. These great HD errors can be estimated with the Fig. 27.

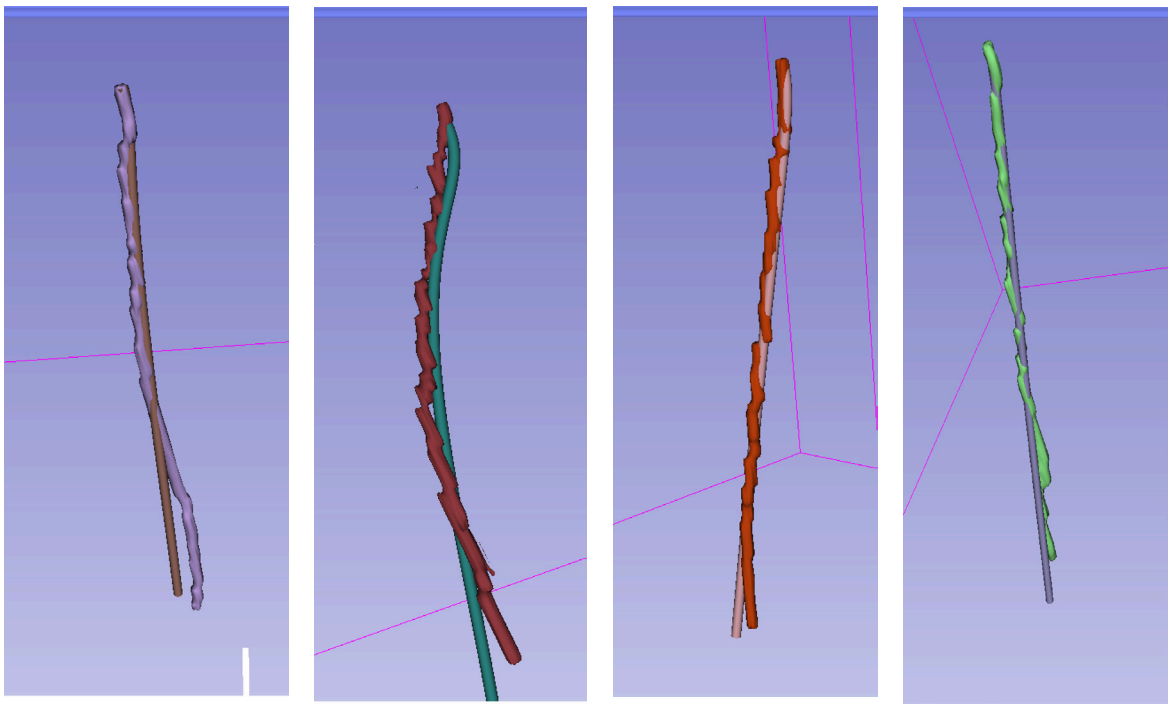

Fig. 27 Respectively needle 5, 6, 8 and 2 (decreasing Hausdorff distance). These picture illustrates high values for the Hausdorff distance.

However, the difficulty of the manual segmentation in this case makes that sometimes, the results of the curved extraction are closer to the reality than the manual segmentation. Indeed, Fig. 28 shows an example with the needle 5, where the manual segmentation by segmenting slice after slice misses the important information provided by the position of the previous points, particularly needed when the needle enter a dark area, and the overall direction of the needle through these points. This information is used as prediction by the algorithm to estimate the position of the next control point.

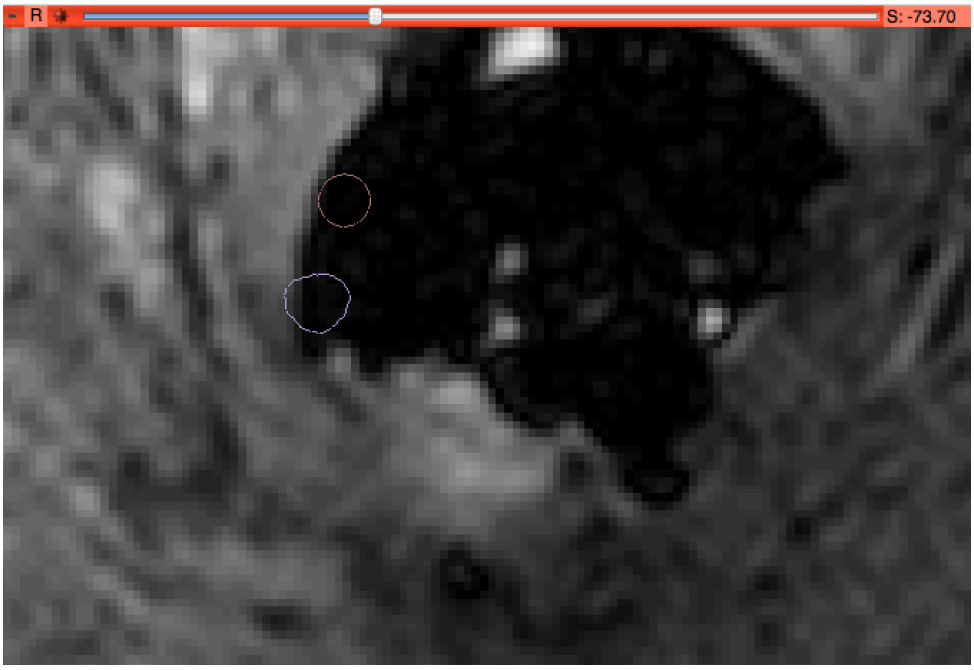

Fig. 28 This figure shows an axial view of the MRI dataset and the cross-section of the manually segmented and the automatically segmented needle 5.

In general, needles around the obturator are really difficult to obtain because of the large dark area where the cross-sections of the needle become invisible. Whereas the human can only guess where it is, the algorithm, using the previously obtained point can estimate with better accuracy where will fall the next following points. In any case, these needles are not the most important to segment because the radiation oncologist can easily distinguish these ones.

Case 3

Table 5: Hausdorff distance results for the case 3. In column 2, Hausdorff distance between manually segmented needles and extracted curved needles. In column 3, standard deviation between manually segmented needles and extracted curved needles. The unit is millimeter.

Needle number	Hausdorff distance	Standard deviation
1	2.91	0.45
2	2.74	0.53
3	2.50	0.39
4	2.86	0.47
5	2.69	0.44
6	2.70	0.46
7	2.18	0.36
8	2.98	0.43

Discussion:

The results obtained for this case are as expected, with a HD error in a 3 mm range. The figure below (Fig. 29) shows an overlay of the algorithm results on the manual segmentation.

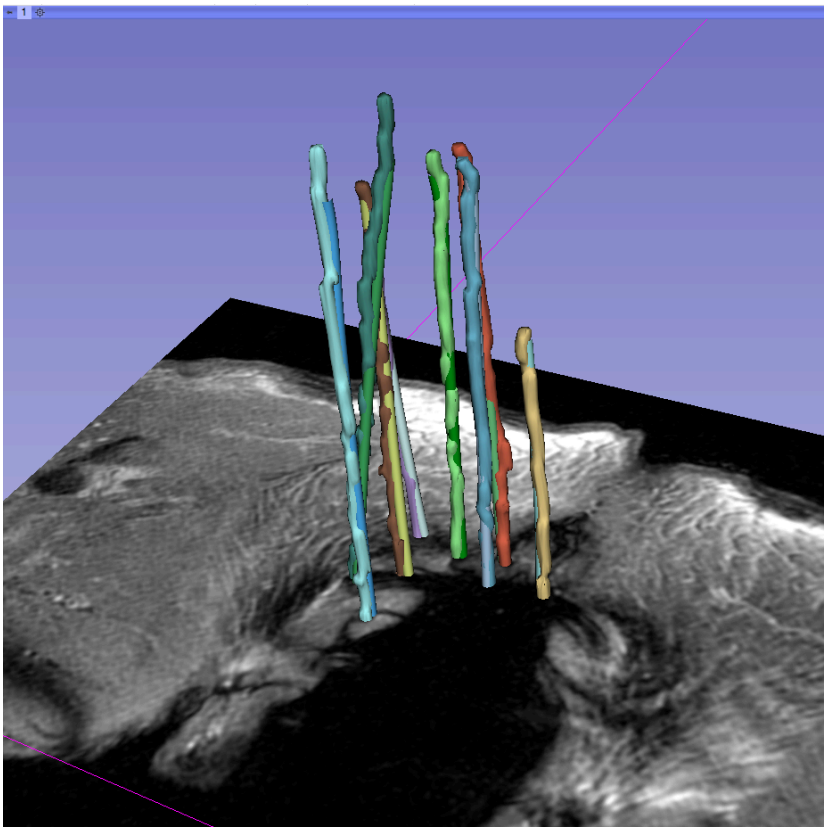

Fig. 29 Comparison of the results of both manual and automatic segmentation in the 3D view for the case 3. Needles are intersected with a 2D axial view.

Case 4

Table 6: Hausdorff distance results for the case 4. In column 2, Hausdorff distance between manually segmented needles and extracted curved needles. In column 3, standard deviation between manually segmented needles and extracted curved needles. The unit is millimeter.

Needle number	Hausdorff distance	Standard deviation
1	1.51	0.24
2	1.86	0.24
3	1.98	0.31
4	4.39	0.59
5	1.97	0.37

Discussion:

The results displayed in the table above illustrate an expected outcome, except for the needle 4. As observed during the previous cases, the error comes mainly from the limitation of the manual segmentation, prone to error, especially in the dark area. The figure below illustrates this point.

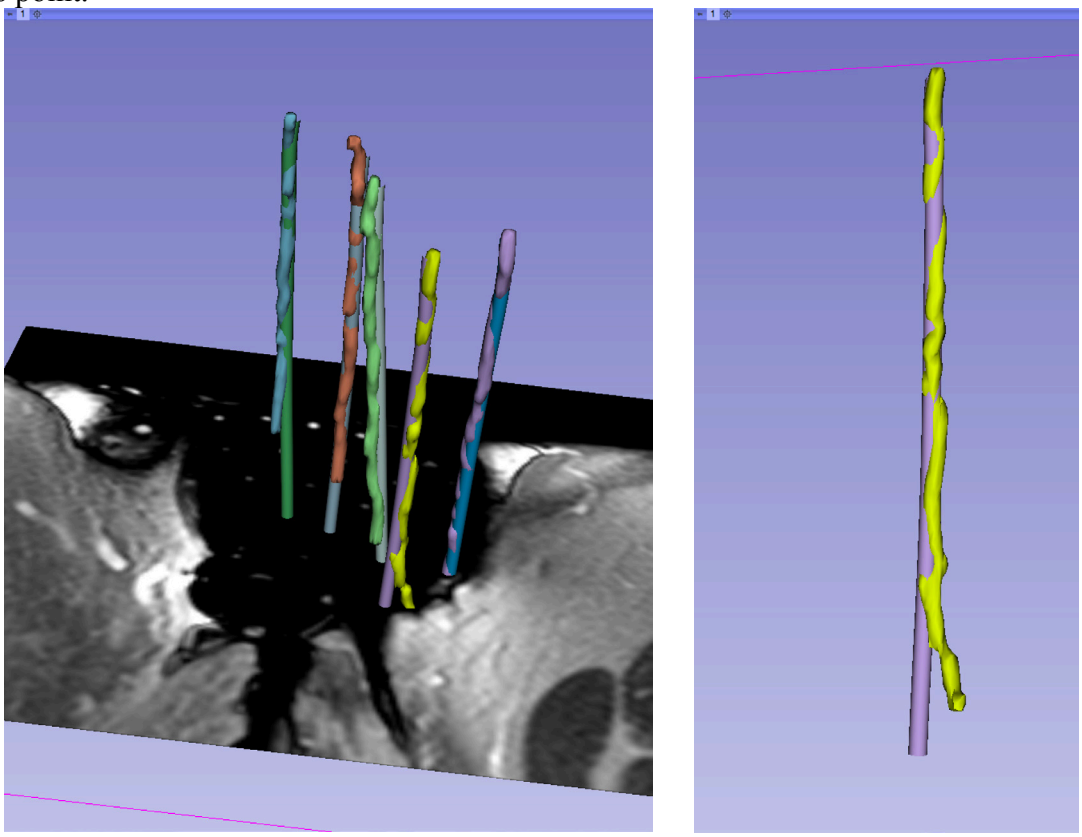

Fig. 30 On the left, the 3D view shows an overlay the algorithmically segmented needles on the manually segmented needles for the case 4. Needles are intersected with a 2D axial view. On the right, illustration of the needle 4, presenting a HD error of 4.39 mm.

Case 5

Table 7: Hausdorff distance results for the case 4. In column 2, Hausdorff distance between manually segmented needles and extracted curved needles. In column 3, standard deviation between manually segmented needles and extracted curved needles. The unit is millimeter.

Needle number	Hausdorff distance	Standard deviation
1	3.48	0.67
2	2.56	0.45
3	2.63	0.39
4	4.95	0.52
5	2.45	0.38
6	10.77	1.78
7	2.26	0.39
8	2.19	0.37

Discussion:

The table above presents results in an expected range, except for needle 4 and 6, having an HD error of 4.95 mm and 10.77 mm

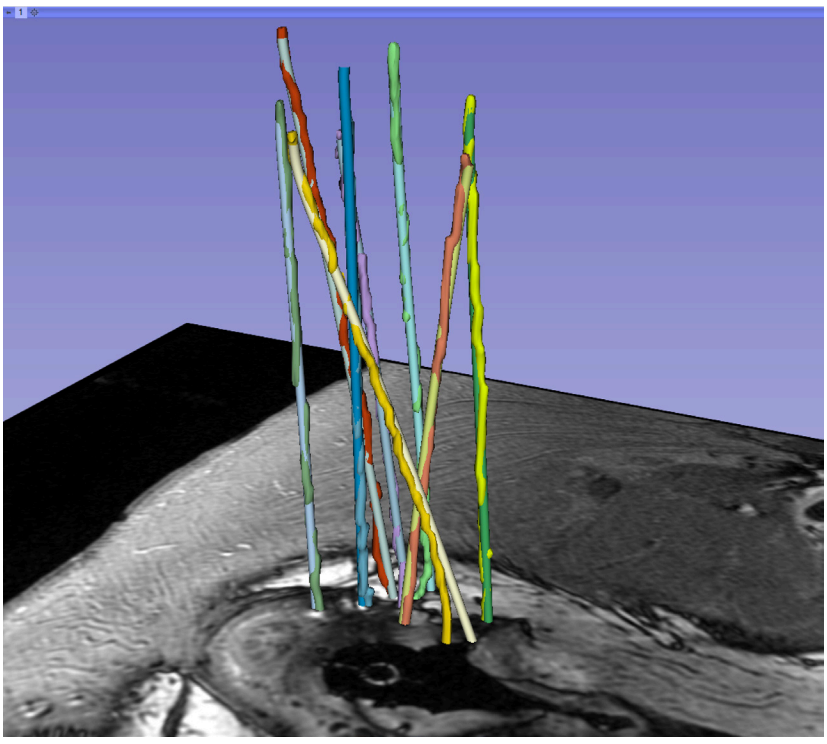

Fig. 31 Comparison of the results of both manual and algorithmic segmentation in the 3D view for the case 5. Needles are intersected with a 2D axial view, close to their base.

However, pairs of needles 4 and 6 show an important disagreement resulting in high HD errors, 495 mm and 10.77 mm respectively. Fig. 32 illustrates this disagreement.

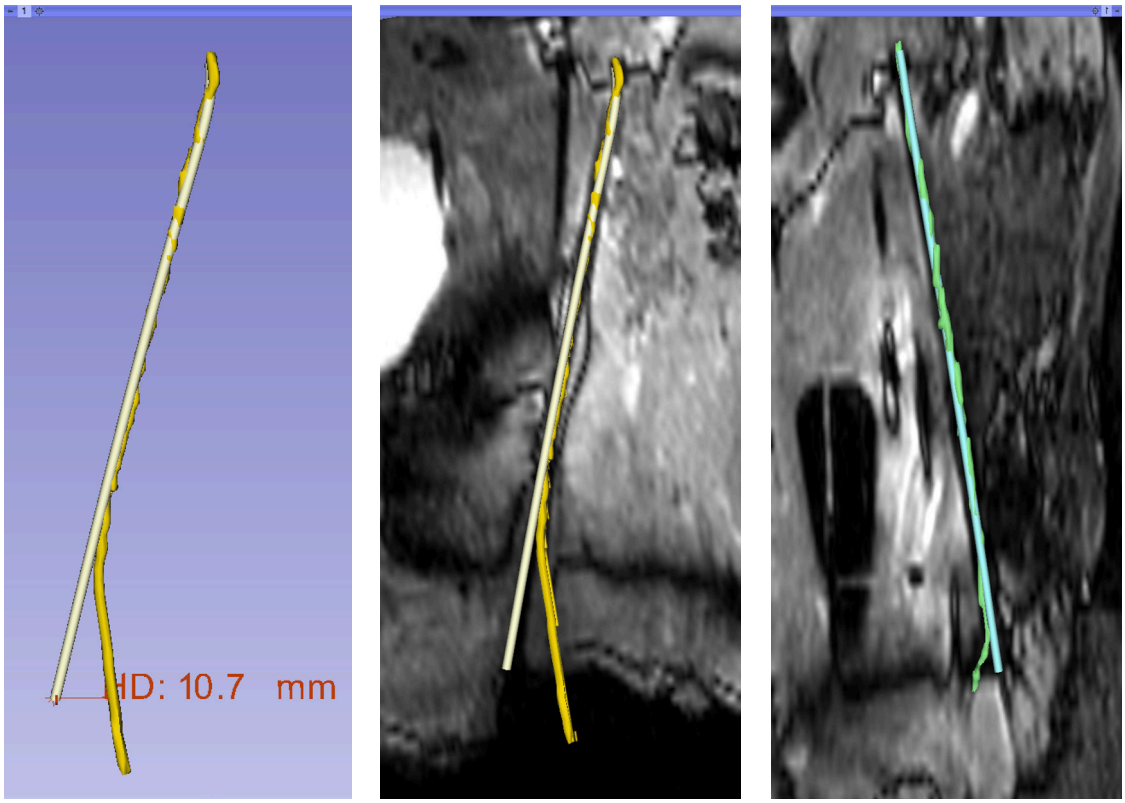

Fig. 32 On the left, the 3D view shows an overlay the algorithmically segmented needle 6 on the manually segmented needle 6 for the case 4. In 3D Slicer, measuring the distance between the closest points that disagree the most, after truncating the difference of length of the needles, gives the same value as obtained in the table above, which is 10.7 mm. In the middle we can observe both models for needle 6 in a reformatted sagittal view, as well as for needle 4, on the right, for which a HD error of 4.95 mm was measured.

For both needles 4 and 6, we can see on the reformatted sagittal view that the manual segmentation deviates from the path of the needle observable in the MRI. Thus, after visual inspection, the algorithmically segmented needles 4 and 6 are considered closer to the reality.

Case 6

Table 8: Hausdorff distance results for the case 6. In column 2, Hausdorff distance between manually segmented needles and extracted curved needles. In column 3, standard deviation between manually segmented needles and extracted curved needles. The unit is millimeter.

Needle number	Hausdorff distance	Standard deviation
1	2.14	0.37
2	2.10	0.38
3	2.46	0.39
4	2.17	0.37
5	2.37	0.42

Discussion:

The results for this case are satisfying. It illustrates particularly the ability of the algorithm to accurately follow the path from the needle tip, even if two tips are very close one from each other, as shown in Fig. 33.

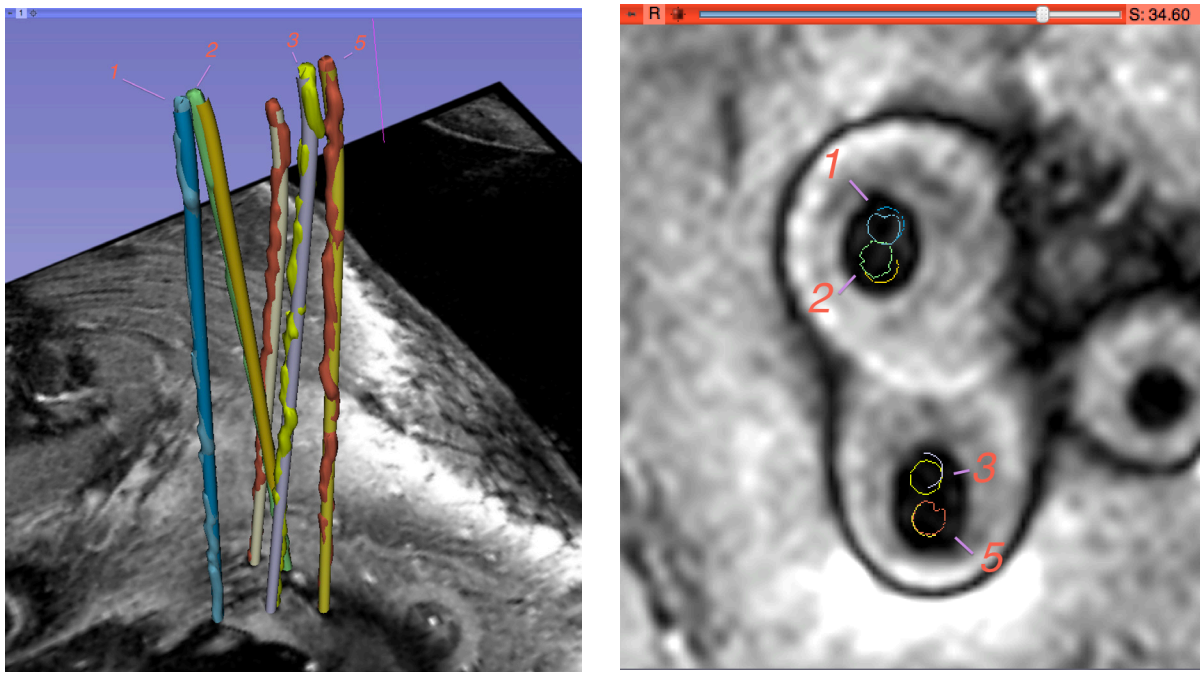

Fig. 33 On the left, 3D view of an overlay of the algorithmically segmented needles on manually segmented needles of case 6. On the right, axial view of pairs of needles 1,2,3 and 5.

Although the needle tip artifact regroups two needles (1 and 2, or 3 and 5), the algorithm is able to differentiate them and provides an accurate segmentation. It is interesting to observe that the needle tip artifacts are around twice bigger than usual for a single needle tip, as shown on the right part of Fig. 33.

Summary of discussion

In these experiments, manual segmentation where expert did slice by slice was used and shown to be error-prone. Moreover, it was not possible to evaluate the accuracy of the needle detection close to the template, because this area appears on MR images, which prevent any manual segmentation slice by slice. To circumvent theses problem, an investigation was done on post-operative CT images obtained for the same patients, but because due to patient movement between MR and CT, a non-rigid registration is required and was beyond the scope of this thesis. The Fig. 34 illustrates the error in registration between MR and CT images for the case 6, after a rigid registration.

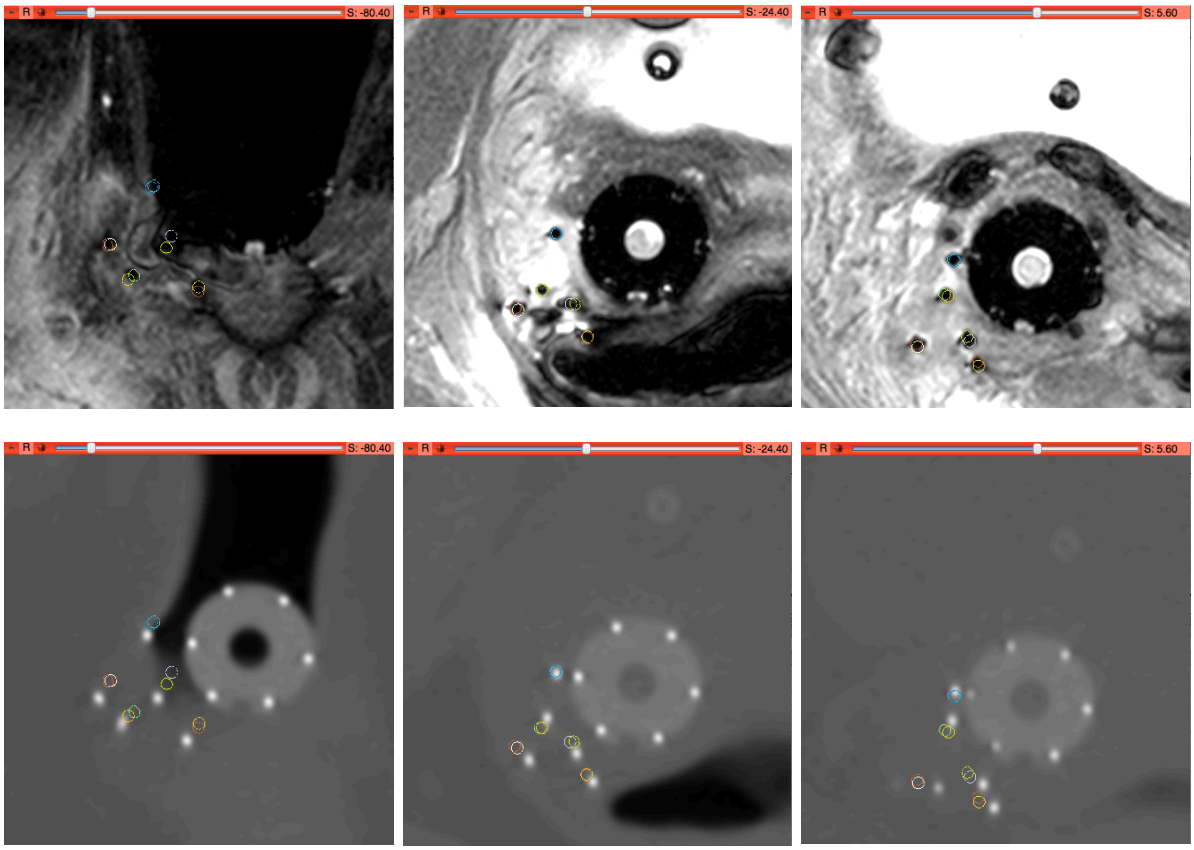

Fig. 34 Comparison in axial views of the position of the needles between MR (first row) and CT images (second row) for the same case, in different slices.

Although the registration was not accurate enough to evaluate directly the Hausdorff distance between pairs of needles from CT and MR images, it was interesting to proceed to an Iterative Closest Point Registration between both sets of needles. The needles from the CT images were extracted by thresholding and applying a unique label to each continuous bright area. Then models were generated from these labels and the Hausdorff distance was computed as for the previous cases. The results are presented in the table below and illustrated with Fig. 35.

Table 9: Hausdorff distance results for the case 6. In column 2, Hausdorff distance between segmented needles of CT by thresholding bright areas, and extracted curved needles of the MR images. In column 3, standard deviation between CT needles and MR extracted curved needles. The unit is millimeter.

Needle number	Hausdorff distance	Standard deviation
1	2.73	0.54
2	1.98	0.44
3	3.84	0.59
4	2.32	0.45
5	3.08	0.63

Results presented in the table above are similar to those obtained after manual segmentation in MR images, but the HD errors are slightly greater. This can be explained with the registration error between MR and CT images, as explained and illustrated above.

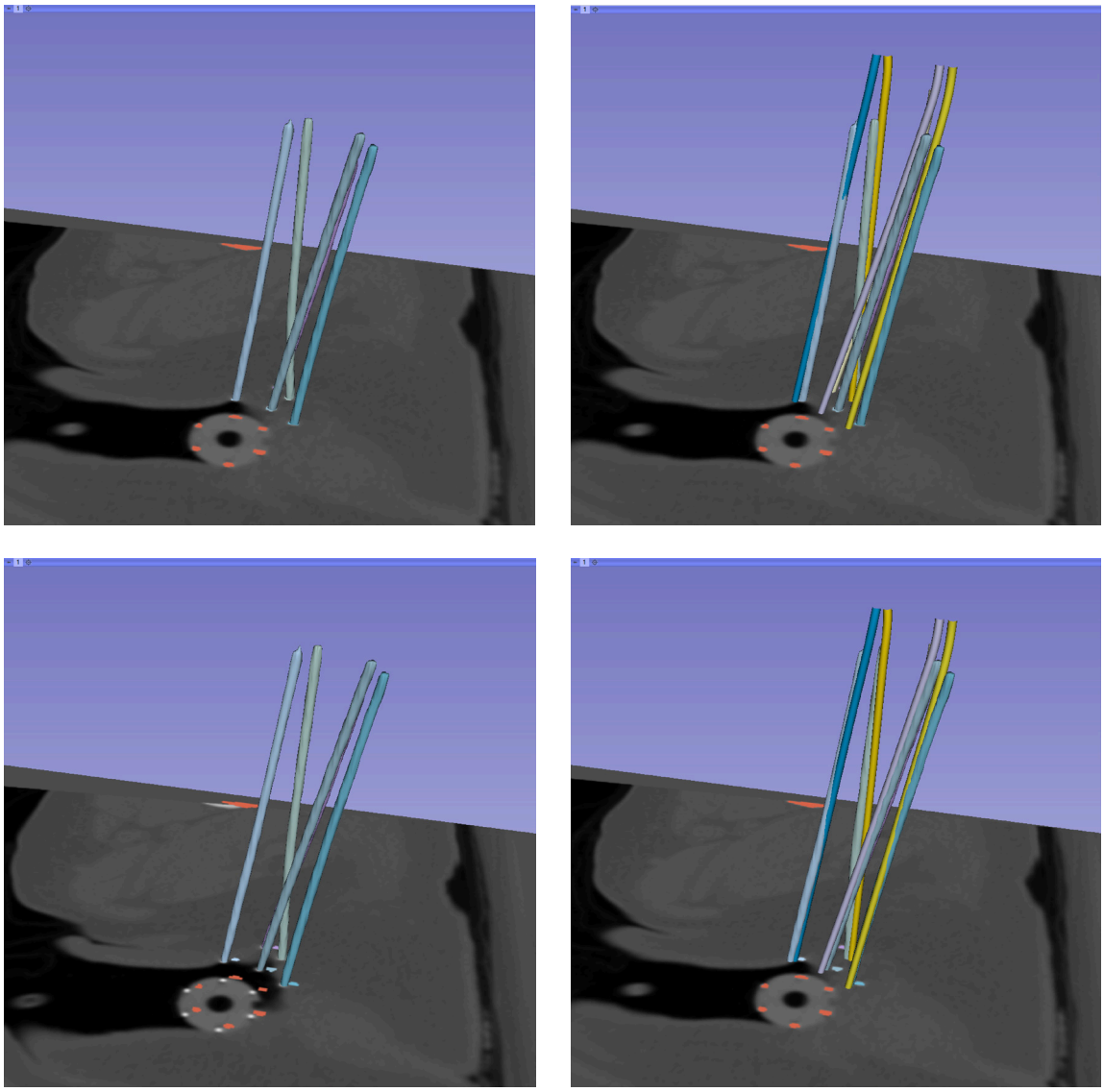

Fig. 35 The first column presents the models of the needle extracted by thresholding in the CT images for the case 6 and the second column shows an overlay of those mentioned models on models of algorithmically segmented in MR images. The first shows the results prior to the Iterative Closest Point registration between point clouds of CT needles and MR needles; the second row shows the result after the ICP registration

On Fig. 35, we can observe an overlay on algorithmically segmented needles on needles extracted by thresholding the CT images, before and after the ICP registration between both sets of needles. Although the registration is still not fully accurate, the results are promising and this method could be used later to evaluate the needle segmentation part. However, the overlays on Fig. 35 show a difference of length of the needles, close to the needle tip. This can be understood by the design of the needles inserted in the catheters during CT imagery. Indeed, a small “spacer”, invisible in CT images, is used to distinguish the needle tip from the rest of the needle. Therefore, a more advanced method for extracting needles from CT images has to be found, other than thresholding continuous bright area. A volume rendering provided below in illustrates this point.

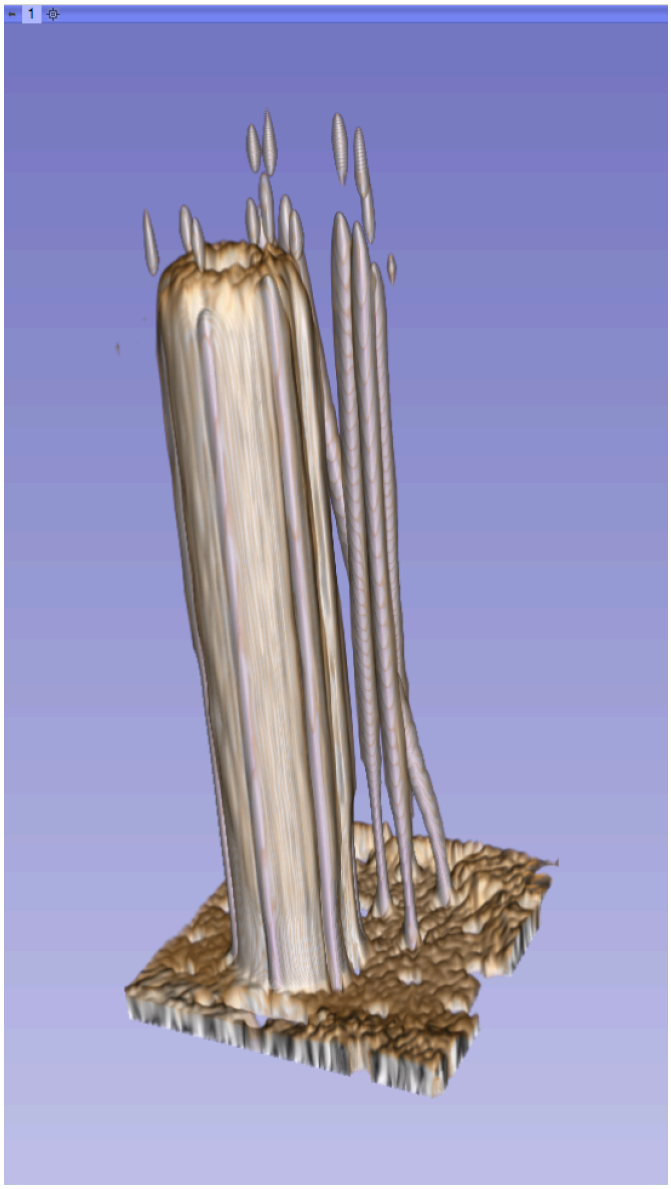

Fig. 36 Volume rendering of the CT images of case 6, cropped around the applicator. Note the needle tips separated from the needle body.

4.2.3 Applicator Registration Experiment

The registration method described in chapter 3 was applied to six T2-weighted MRI datasets acquired using a Siemens 3T scanner in the Advanced Multimodality Image Guided Operating (AMIGO) suite at Brigham and Women's Hospital.

4.2.4 Applicator Registration Results: Comparison between different Methods on six Patient MRI Datasets

The following evaluation includes previously used registration methods including different segmentation methods as the GrowCut segmentation [22], which asks the user to draw rough gestures inside and outside the region to segment. The “template-only” registration represents the registration method using only the information provided by the template. “Automatic-segmentation” represents the segmentation method described in chapter 3.

To quantify the results of the registration, the Root Mean Square error was computed between corresponding points of a manually obtained registration (ground truth), and of registration methods described above. The point sets are the points composing the CAD model of the gynecological applicator, evaluated after transformation with the transformation matrix of the registration.

To be noted, the numbering of the case is not related to the one of the case previously used in the needle segmentation evaluation.

Table 10: Evaluation of the RMS error of the registration between corresponding points of a manually obtained registration, and of the registration named by the column header. The first column presents the evaluation results of the registration state after the first initial landmark registration. The results are in millimeters.

Case	Initial registration	Template only	GrowCut	Automatic segmentation
1	21.08	2.01	1.45	3.57
2	18.24	24.61	7.96	6.70
3	7.98	8.46	2.92	7.31
4	8.51	12.17	0.84	6.10
5	17.60	16.75	7.11	0.71
6	22.58	19.74	3.00	1.38
Average	16.00	13.96	3.88	4.30
Standard deviation	6.28	8.14	2.96	2.83

A significant improvement in accuracy was obtained, compared to the previous (template-only) registration method. The RMS error dropped by more than 70% (from 14 mm to 4 mm). Part of following results were submitted to the American Brachytherapy Society 2013 Annual Meeting [25].

Table 11: Computation time for the different registration methods, in seconds.

Cases	Template only	GrowCut	Automatic segmentation
1	26	150	25
2	42	212	31
3	28	463	33
4	36	190	27
5	25	120	29
6	33	273	21
Average	32	235	27
Standard Deviation	6.52	123.65	4.39

If the GrowCut segmentation and the "Automatic segmentation" give similar results (RMS error average of 3.88 mm and 4.30 mm), the computation time, of the last one is in average more than eight times shorter. The computation time being a critical parameter during a clinical case, the automatic segmentation method has been chosen. Moreover, no user interaction is needed.

5 Conclusion and Future Work

In this thesis, an open-source and multiplatform software module for labeling catheters in magnetic resonances images of interstitial gynecological brachytherapy cases was presented. The introduced software module uses methods for model-to-image registration and image segmentation. The first method, model-to-image registration is performed in two steps: Hough-transform finds the landmarks used for an initial registration and segmentation of the images of the template and obturator (parts of the gynecological applicator) which provides the additional information needed to refine the registration. The second method, needle segmentation was introduced to extract curved as well as straight needles in MR images. Adding constraints coming from the needle mechanical properties to an iterative algorithm looking for points on the needle path, the algorithm is able to segment a needle in less than a second after the user clicks on the needle tip. Then a comparison between registered models and segmented models leads to the labeling information.

The presented methods have been tested on two phantom MRI datasets as well as on 6 patients MRI datasets. The ground truth of the registration of the gynecological applicator CAD model has been done manually by expert visual inspection and was compared to the result of the automatic applicator registration, yielding an average RMS error of 4.3 mm. The ground truth of the needle extractions was done by a physician with experience in segmentation of gynecological MRI datasets and was compared with the needle segmentation algorithm results, yielding an average Hausdorff distance in a 3 mm range with a standard deviation value in a 0.5 mm range.

There are several areas of future work. First, the accuracy of the labeling needs to be quantified, although the empirical results are satisfying so far. Then, for example, a cylindrical shape detection algorithm as presented by Rabbani et al. in 2005 [26] could be used to improve the segmentation of the obturator, which is cylindrical, in the refined registration step. The algorithm for the needle detection could be enhanced by adding domain constraints coming from already segmented structures, like the obturator for example. Additionally, the method can be enhanced with statistical information about the signal-to-noise ratio of the slices used to optimize the needle segmentation parameters.

Furthermore, the needle segmentation step could be entirely automated with a needle tip artifact detection step giving the only needed input to the algorithm, which is the needle tip. However, this artifact ("*figure 8*" shape) being subject to many changes because due to its shape relative to the MR sequence used, the material of the needle or properties of the tissue around the needle, this solution seems not to be robust enough on the long-term. Instead, it could be possible to detect dark areas corresponding to needle cross-sections, in many axial slices, (using intensity threshold and to filter the results depending on their area, keeping those close to $\pi * 1^2 \approx 3\ mm^2$), then to compute the needle detection algorithm from these cross-sections and finally to cross-check the results together, keeping only the ones overlapping in a certain minimal range.

Bibliography

1. Siegel, R., D. Naishadham, and A. Jemal, *Cancer statistics, 2012.* CA: a cancer journal for clinicians, 2012.

2. Sturdza, A. and R. Pötter, *Outcomes Related to the Disease and the Use of 3D-Based External Beam Radiation and Image-Guided Brachytherapy*

Gynecologic Radiation Therapy, A.N. Viswanathan, et al., Editors. 2011, Springer Berlin Heidelberg. p. 263-282.

3. Beriwal, S., et al., *American Brachytherapy Society consensus guidelines for interstitial brachytherapy for vaginal cancer.* Brachytherapy, 2012. **11**(1): p. 68-75.

4. Gupta, V., *Brachytherapy-past, present and future.* Journal of Medical Physics, 1995. **20**(2): p. 31.

5. Lee, C. and G. Lowe, *Isotopes and delivery systems for brachytherapy.* Radiotherapy in Practice-Brachytherapy, 2011: p. 5.

6. Cleary, K. and T.M. Peters, *Image-guided interventions: technology review and clinical applications.* Annu Rev Biomed Eng, 2010. **12**: p. 119-42.

7. Lewin, J.S., *Interventional MR imaging: concepts, systems, and applications in neuroradiology.* AJNR Am J Neuroradiol, 1999. **20**(5): p. 735-48.

8. DiMaio, S.P., et al., *Needle artifact localization in 3T MR images.* Stud Health Technol Inform, 2006. **119**: p. 120-5.

9. Ding, M., H.N. Cardinal, and A. Fenster, *Automatic needle segmentation in three-dimensional ultrasound images using two orthogonal two-dimensional image projections.* Medical Physics, 2003. **30**: p. 222.

10. Okazawa, S.H., et al., *Methods for segmenting curved needles in ultrasound images.* Med Image Anal, 2006. **10**(3): p. 330-42.

11. Kalman, R.E., *A new approach to linear filtering and prediction problems.* Journal of basic Engineering, 1960. **82**(1): p. 35-45.

12. Velastin, S. and C. Xu, *Image feature extraction using a method derived from the Hough transform with extended Kalman filtering.* Advances in Image and Video Technology, 2007: p. 191-204.

13. Mahalanobis, P.C. *On the generalized distance in statistics*. in *Proceedings of the National Institute of Sciences of India*. 1936. New Delhi.

14. Dalca, A., et al., *Segmentation of nerve bundles and ganglia in spine MRI using particle filters.* Medical Image Computing and Computer-Assisted Intervention–MICCAI 2011, 2011: p. 537-545.

15. Tibrewal, R., *Image-Based Needle Guidance for MR-Guided Interstitial Gynecological Brachytherapy in AMIGO.* Technische Universität München, Biomedical Computing, 2012.

16. Zhang, Z., *Iterative point matching for registration of free-form curves and surfaces.* International journal of computer vision, 1994. **13**(2): p. 119-152.

17. Kikinis, R. and S. Pieper, *3D Slicer as a tool for interactive brain tumor segmentation.* Conf Proc IEEE Eng Med Biol Soc, 2011. **2011**: p. 6982-4.

18. Fedorov, A., et al., *3D Slicer as an image computing platform for the Quantitative Imaging Network.* Magn Reson Imaging, 2012. **30**(9): p. 1323-41.

19. Gao, Y., N. Fahrat, and G. Pernelle, *Needle labeling for interstitial brachyteraphy.* Fifth National Image Guided Therapy Workshop, 2012.

20. Kapur, T., et al., *3-T MR-guided brachytherapy for gynecologic malignancies.* Magn Reson Imaging, 2012. **30**(9): p. 1279-90.

21. Horn, B.K.P., *Closed-form solution of absolute orientation using unit quaternions.* JOSA A, 1987. **4**(4): p. 629-642.

22. Vezhnevets, V. and V. Konouchine. *GrowCut: Interactive multi-label ND image segmentation by cellular automata*. in *Proc. of Graphicon*. 2005.

23. Morrison, D.S. and W.J. Heilman, *Transparent gel candles* U.S. Patents, Editor 1997, Pennzoil Products Company: United States.

24. Huttenlocher, D.P., G.A. Klanderman, and W.J. Rucklidge, *Comparing images using the Hausdorff distance.* Pattern Analysis and Machine Intelligence, IEEE Transactions on, 1993. **15**(9): p. 850-863.

25. Pernelle, G., et al., *Robust Applicator Registration for Interstitial Gynecologic Brachytherapy.* ABS 2013 Annual Meeting, 2013. **(submitted)**.

26. Rabbani, T. and F. Van Den Heuvel, *Efficient hough transform for automatic detection of cylinders in point clouds.* ISPRS WG III/3, III/4, 2005. **3**: p. 60-65.

List of Figures

Appendix

Fifth National Image Guided Therapy Workshop, September 21, 2012, Boston, MA

Needle Labeling for Interstitial Gynecological Brachytherapy

Yi Gao[1], Nabgha Farhat[1], Neha Agrawal[1], Guillaume Pernelle[1], Xiaojun Chen[1], Jan Egger[1], Tyler Blevins[1], Sylvain Bouix[1], Allen Tannenbaum[2], William Wells[1], Ron Kikinis[1], Ehud Schmidt[1], Akila Viswanathan[1**] and Tina Kapur[1**]
[1]Brigham and Women's Hospital, [2]Boston University, **Joint Senior Authorship

Purpose – During the process of needle insertion for interstitial gynecologic brachytherapy, the needles may bend secondary to tissue deflection. Variability in tissue resistance may arise from fat, water, bone or muscle coursed through in the path of the needle. In this work we provide a fast and accurate method to extract and display needles from MR images acquired during MR-guided gynecological cancer brachytherapy. Compared to CT, needle artifacts are less easily identifiable in T2w MR, the sequence of choice for visualizing gynecologic cancer. In previous work [1], we introduced the use of a customized SSFP MR sequence to enhance needle artifacts in these procedures, and in this work we provide a post-processing method that reliably and accurately extracts the needles from images acquired using these SSFP MR images.

Methods – The user is asked to provide two pieces of information in order to initiate the needle extraction tool. First, the user is asked to draw a region in one of the transverse slices where all the needles pass through. For example, when a Syed Neblett template is used and is visible in the scan, this region can be the approximate outer boundary of the template. Then, the user is asked to scroll to a superior transverse slice close to the tip of the needles, and identify the cross sections of the needles. The algorithm then takes over to extract the needles in the image. Mathematically, we denote the MR image as a function $I:\Omega\rightarrow R$ where Ω is the field of the view of the image. Accordingly, denote the voxel positions drawn by user for the template as $B = \{b_i \in \Omega;\ i = 1, \ldots, N\}$ and the voxel positions for the needles as $D = \{d_i \in \Omega;\ i = 1, \ldots, M\}$. Then, the Hessian image $H: \Omega\rightarrow S^{3\times3}$ is computed. The eigen system of the 3×3 matrix defines a Conformal Euclidean metric on Ω [2]. A straight line is then computed from each needle label region among $d_{1,\ldots,M}$, to the template region B. By doing this, an optimal line is obtained for each needle, which is regarded as the needle. The algorithm is implemented in C++ language.

Results – This needle extraction tool has been used to segment needles on 6 SSFP MR images. The running time, from user input to final results, is less than one minute to extract up to 20 needles. The figure on the right shows the results of the needle extraction algorithm on three cross-sections (top), and rendered in 3D (below). Results have been visually compared very favorably to manual needle extraction by a physician, and will be quantified in future work.

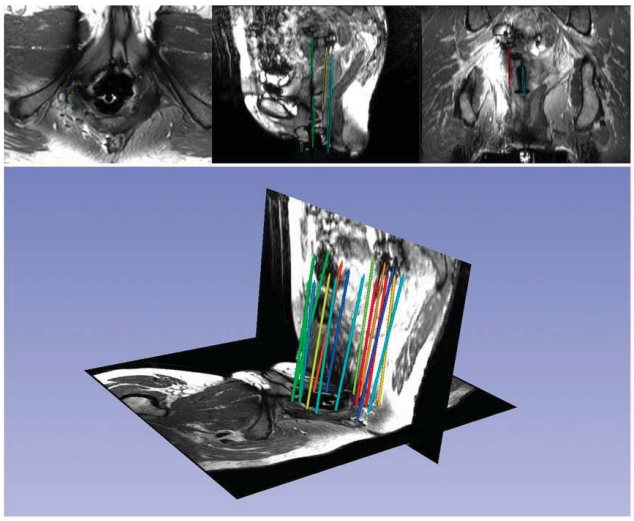

Conclusions – In this work we have a novel algorithm to extract gynecologic brachytherapy needles from SSFP MR imagery. The algorithm requires simple inputs from the user based on which 3D models of the needles are constructed in a time frame that is acceptable for intra-procedural guidance. Future work includes (1) modeling the bending of needles (2) quantitative comparison of results to manual extraction of needles from MR, as well as to CT images.

Acknowledgements
This work was supported by NIH grants R03EB013792, P41EB015898, U54EB005149, and members of the AMIGO and Slicer communities.

References
[1] Kapur, T., Egger, J., Damato, A., Schmidt, E.J. & Viswanathan, A.N., 3-T MR-guided brachytherapy for gynecologic malignancies. Magnetic Resonance Imaging, Elsevier, in Press, 2012.
[2] Kichenassamy, S., *et al.*, Arch. Rational Mechanics and Analysis, 134(3):275–301, 1996.

RobustApplicator Registration for Interstitial Gynecologic Brachytherapy

Guillaume Pernelle[a,b*], Jan Egger, Ph.D.,Ph.D.[b*],Carolina Vale [c], Xiaojun Chen, Ph.D.[b],Franz Irlinger, Ph.D.[a], Tim C. Lueth, Ph.D.[a], Ron Kikinis, M.D.[b], William Wells, Ph.D.[b], AkilaViswanathan, M.D., M.P.H.[b**], Tina Kapur, Ph.D.[b**]
[a]Technical University of Munich (TUM),[b] Brigham and Women's Hospital, Boston,[c]Faculty of Science,University of Lisbon
*Joint First Authorship, **Joint Last Authorship

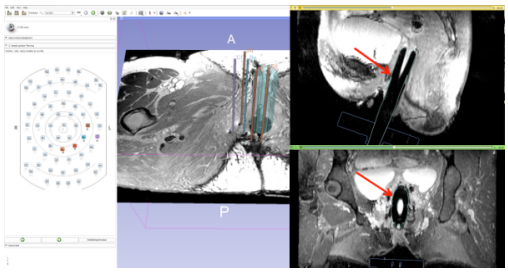

Figure 1. Interface allowing simulating insertion of needles (left image). Result of the refined ICP registration of the obturator and the template (right images).

Purpose–We present a method for robust localization of the Syed-Neblett gynecologic brachytherapy applicator in intra-operative Magnetic Resonance (MR) imagery by alignment with its computer aided design (CAD) model. This alignment allows us tovisualize "virtual needles" prior to the actual insertion.

Methods–Previously, we reported initial development of a software module named "iGyne" using the free and open source software platform*3D Slicer* (http://www.slicer.org). Within iGyne, we reported a registration method based on user-initialized correspondences between 3 points, followed by Iterative Closest Points (ICP) surface registration of the Syed-Nebletttemplate. In this work, we provide additional information to the registration method by including the obturator in the process. Specifically, we have added to the iGyne software module a step that allows the user to draw rough "gestures" – one inside the obturator, and one outside it – and then uses the *GrowCut* algorithm to automatically segment the obturator from the rest of the image. As an intermediate step, a 3D model is generated from the segmented label map of the obturator, and then an ICP registration is used to register the surfaces of both the template and obturator CAD models against their segmentations in the MR images.

Results–We applied this method to six T2-weighted MRI datasets acquired using a Siemens 3T scanner in the Advanced Multimodality Image Guided Operating (AMIGO) suite at Brigham and Women's Hospital. We computed the quadratic mean distance (Root Mean Square error) between corresponding resulting points of a manually obtained registration (ground truth), and of both registration methods described above. We obtained a significant improvement in accuracy compared to the previous (template-only) registration method. The RMS error dropped by more than 70% (from 14mm to 4mm).The Figure illustrates a representative case.To support open science, all data sets used in this study have been anonymized and made available freely and publiclyathttp://www.spl.harvard.edu/publications/item/view/2227. Potential users of this data are requested to cite Kapur et al. MagnReson Imaging 2012 that provides the overall vision of gynecological brachytherapy in AMIGO.

Conclusions– In this contribution, we present a registration method for CAD models ofthe Syed-Neblett template and the obturator for interstitial gynecologic brachytherapy that is available in the iGyne module of the open source software package 3D Slicer. Areas of immediate future work include the further improvements to the accuracy of the method so that it is less than 2mm Root Mean Square error.

Acknowledgements
This work was supported by NIH grants R03EB013792, P41EB015898, U54EB005149, and members of the AMIGO and Slicer communities.

Glossary

ABS	American Brachytherapy Society
AMIGO	Advanced Multimodality Image Guided Operating Suite
b-SSFP	Balanced Steady-State Free Precession
BWH	Brigham and Women's Hospital
CHT	Circular Hough Transform
CT	Computed Tomography
CTK	Common Toolkit
CTV	Clinical Target Volume
DVH	Dose Volume Histogram
EBRT	External Beam Radiation Therapy
EKF	Extended Kalman Filter
FSE	Fast-Spin-Echo
GHT	General Hough Transform
GRE	Gradient Echo
Gy	Gray
GUI	Graphic User Interface
HD	Hausdorff Distance
HDR	High Dose Rate
HMS	Harvard Medical School
HR	High-Risk
IR	Intermediate-Risk
IRB	Institutional Review Board
ITK	Insight Segmentation and Registration Toolkit
LDR	Low Dose Rate
MDR	Medium Dose Rate
MIT	Massachusetts Institute of Technology
MRI	Magnetic Resonance Imaging
NA-MIC	National Alliance for Medical Image Computing
OAR	Organs-At-Risk
PET	Positron Emission Tomography
PTV	Planning Target Volume
SHT	Standard Hough Transform

VTK Visualization Toolkit